Spin relaxation, diffusion, and Edelstein effect in chiral metal surface

Yuta Suzuki [*]
Department of Physics, University of Tokyo, Bunkyo, Tokyo 113-0033, Japan

Yusuke Kato [†]
Department of Basic Science, University of Tokyo, Meguro-ku, Tokyo 153-8902, Japan

(Received 31 December 2022; accepted 13 March 2023; published 27 March 2023)

We study electron spin transport at the spin-splitting surface of chiral-crystalline-structured metals and the Edelstein effect at the interface, by using the Boltzmann transport equation beyond the relaxation time approximation. We first define spin relaxation time and spin diffusion length for two-dimensional systems with anisotropic spin-orbit coupling through the spectrum of the integral kernel in the collision integral. We then explicitly take account of the interface between the chiral metal and a nonmagnetic metal with finite thickness. For this composite system, we derive analytical expressions for efficiency of the charge current–spin current interconversion as well as other coefficients found in the Edelstein effect. We also develop the Onsager reciprocity in the Edelstein effect along with experiments so that it relates local input and output, which are respectively defined in the regions separated by the interface. We finally provide a transfer matrix corresponding to the Edelstein effect through the interface, with which we can easily represent the Onsager reciprocity as well as the charge-spin conversion efficiencies we have obtained. We confirm the validity of the Boltzmann transport equation in the present system starting from the Keldysh formalism in supplemental material. Our formulation also applies to the Rashba model and other spin-splitting systems.

DOI: 10.1103/PhysRevB.107.115305

I. INTRODUCTION

Over the last three decades, there has been considerable interest in spin generation, spin detection, and spin transport in surfaces, interfaces, and noncentrosymmetric crystal structures. One of the well-studied phenomena in this field is charge-spin interconversion by the Edelstein effect (EE) [1–3] and its reciprocal effect, i.e., the inverse Edelstein effect (IEE) [4,5]. They have been explored both theoretically [6–9] and experimentally at the Rashba spin-splitting surface [10–12] or topological insulator surfaces [13,14], where spin and momentum are perpendicularly coupled.

Recently, current-induced magnetization and its inverse effect have been observed in chiral-crystalline-structured metals, bringing a new perspective to the field of spin transport. Experiments on the paramagnetic phase in a chiral metal $CrNb_3S_6$ [15,16] and nonmagnetic chiral metals $TaSi_2$ and $NbSi_2$ [17,18] with the D_6 (622) point group display parallel coupling of charge current and spin polarization in the direction of the principal axis, associated with an external electric field or spin current injection to the metals. The relative sign of the current and polarization depends on the chirality of the metal, which makes sure that the observed effects are unique to the chiral crystalline structure [19].

The parallel current-induced magnetization, allowed in chiral systems [20,21], may be understood based on a microscopic spin-orbit coupling (SOC), which includes parallel coupling of spin and momentum around the Γ point [22]. However, there are two distinctive features within spin polarization in the chiral metals: high efficiency of the charge-spin conversion and long-range spin transport. They make this effect intriguing but challenging from a theoretical standpoint. For the former feature, the current-induced magnetization is reported to be so large [16] that the spin polarization has been detected simply by attaching nonmagnetic metals onto the surface of chiral metals [15,17,18]. That process has been phenomenologically explained as a spin diffusion across the interface. Such a large polarization is not shown in elemental tellurium [20,23], and may be characteristic to the chiral metals. For the latter feature, the chiral metals are reported to have robust spin polarization, which persists over millimeters even in the absence of net charge current. That length scale is much longer than typical spin diffusion length in metals, and the origin of such nonlocality is still under discussion [24,25].

With these backgrounds, highly required is a theoretical scheme (a) having a firm basis and (b) capable of dealing with nonlocal spin transport in the presence of anisotropic SOC as well as (c) the charge-spin interconversion through an interface between a chiral metal and nonmagnetic achiral metal with finite thickness. We aim to present a prototypical model satisfying those conditions.

In this paper, we study spin and charge transports in two-dimensional (2D) metals with an anisotropic SOC with weak disorder due to nonmagnetic impurities in Sec. II [Fig. 1(a)] and spin transport between this 2D system, and a three-dimensional nonmagnetic metal with a finite thickness in

[*]suzuki@vortex.c.u-tokyo.ac.jp
[†]yusuke@phys.c.u-tokyo.ac.jp

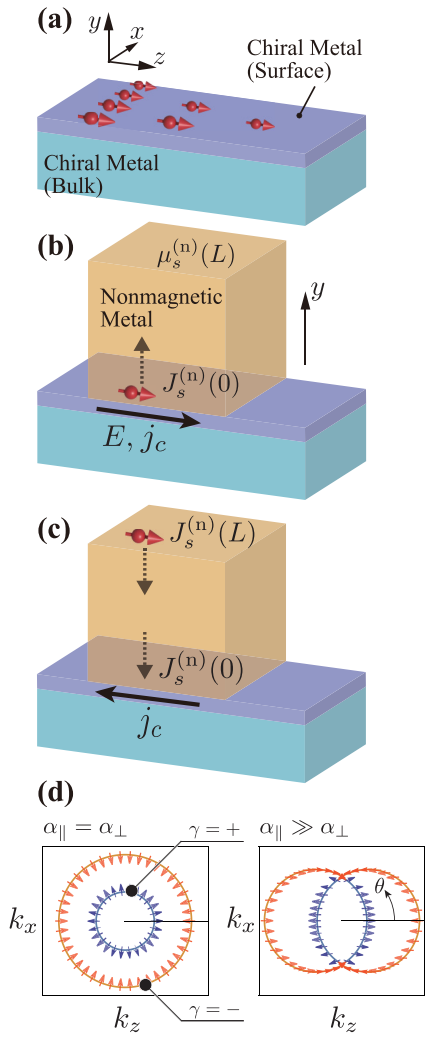

FIG. 1. Schematic pictures of temporal spin relaxation and spatial spin diffusion [(a)] at the chiral metal surface, direct Edelstein effect [(b)], inverse Edelstein effect [(c)] across the interface, and radial spin texture of the Fermi contours at the surface [(d)]. Arrows denote spin polarization. (d) The spin-orbit coupling is set to be isotropic (left) and anisotropic (right, $\delta = \pi/64$) with the same strength of SOC $\alpha/v_F\hbar = 0.6$.

Sec. III [Figs. 1(b), 1(c)]. The 2D systems can be regarded as a chiral metal surface, a mimic of three-dimensional chiral metals, or an equivalent to the Rashba system or a Rashba-Dresselhaus system via 90-degree rotation in spin space. We model the interface as a tunnel junction with a nonmagnetic bulk metal that follows the spin diffusion equation [26] (Sec. III A). We make full use of the Boltzmann transport equation (BTE) beyond the relaxation time approximation, which provides accurate transport properties when the 2D electron system at the surface is clean enough or spin splitting caused by SOC is large enough [27]. That is just the case when the Edelstein effect becomes evident. Derivation of the BTE based on the Keldysh formalism is given in Sec. S4 of the Supplemental Material [27] (see, also, Refs. [28–39] therein).

Our contributions are threefold: (i) We have defined spin diffusion length for each spin component and diffusion direction in the chiral metal surface, as well as spin relaxation time for each spin component (Secs. II B and II C). Our definition does not rely on spin-dependent chemical potential, which is conventionally employed but is ill-defined under strong SOC. We have also clarified how these spin relaxation time and diffusion length depend on the anisotropy of the SOC, since some chiral crystals have strongly anisotropic SOC, such as elemental tellurium [23]. (ii) We have obtained analytical expressions for the conversion efficiencies at the chiral metal interface, from charge current to spin current, and vice versa (Sec. III B). Here in accordance with the spin-current-injection experiment, we take account of a finite thickness of the three-dimensional (3D) nonmagnetic metal and consider the spin current density at an edge of the 3D metal as a controllable parameter. Such a realistic description has been done by this study, in contrast to previous theoretical studies on the EE and IEE [5,8,9]. The Rashba-Edelstein effect at interfaces also follows our analytical results, which practically supports a phenomenological model proposed by Ref. [40]. (iii) We have developed the Onsager reciprocity between the EE and IEE, originally given by Ref. [5] at a surface, to the interface system (Sec. III C). Along with experiments, the reciprocity we found relates local input and output, which are defined in the regions separated by the interface. The reciprocity as well as the charge-spin conversion efficiencies are finally summarized in terms of a transfer matrix method, which reflects the nature of the composite systems.

II. SPIN TRANSPORT IN CHIRAL METAL SURFACE

A. Formulation for the surface

We start with a two-band effective model for electrons in the chiral metal surface

$$H^{2D}(\boldsymbol{k}) = \frac{\hbar^2\left(k_z^2 + k_x^2\right)}{2m} + H_{SO}, \tag{1}$$

with z, x axes in the surface plane. The second term of SOC is described as

$$H_{SO} = \alpha_\parallel k_z \sigma_z + \alpha_\perp k_x \sigma_x = \boldsymbol{g}(\boldsymbol{k}) \cdot \boldsymbol{\sigma}, \tag{2}$$

with two SOC parameters $(\alpha_\parallel, \alpha_\perp) = (\alpha\cos\delta, \alpha\sin\delta)$, standing for its strength α and anisotropy δ. We here put the momentum $\boldsymbol{k} = (k_z, k_x) = (k\cos\theta, k\sin\theta)$ and spin denoted by Pauli matrices $\boldsymbol{\sigma} = (\sigma_z, \sigma_x)$.

The SOC model we provide in Eq. (1) is suitable for describing slowly varying spin polarization in the 2D system, i.e., spin relaxation time much longer than momentum relaxation time and spin diffusion length much longer than mean free path. Indeed, if we take anisotropic limit $\delta \to 0$ or $\delta \to \pi/2$, spin σ_z or σ_x becomes a pseudoconserved quantity, which leads to almost-constant spin polarization in the chiral metal surface. We thus write the SOC term H_{SO} with two different parameters ($\alpha_\parallel$ and $\alpha_\perp$), while we assume the kinetic energy part to be isotropic for simplicity.

That parallel coupling of spin and momentum (2) is designed to simulate the observed spin polarization at the surface of the chiral metals that is parallel to charge current [15,17,18]. That parallel coupling terms may result from the bulk inversion asymmetry of the chiral-crystalline structure, in the same manner as the Dresselhaus SOC in zinc blende structure reflected in SOC at the interface [41,42]; that SOC

is obtained after we eliminate the freedom of motion along the y axis normal to the surface from the hedgehog-like SOC $\alpha_\parallel k_z\sigma_z + \alpha_\perp(k_x\sigma_x + k_y\sigma_y)$ around the Γ point in the bulk chiral metals with the D_6 (622) point group [22]. The spin splitting due to the hedgehog-like SOC in $TaSi_2$ and $NbSi_2$ has been observed by de Haas–van Alphen measurements [43]. The microscopic origin of the hedgehog-like SOC in the bulk of chiral crystals has recently been revealed in terms of atomic-scale multipoles [44].

The surface model may also require the Rashba SOC [45] and other SOC terms due to the structural inversion asymmetry, but the whole SOC in that case is also reduced to the same expression as Eq. (2) under appropriate rotations (Sec. S1 of the Supplemental Material [27]). In particular, simple Rashba SOC corresponds to an isotropic case of that coupling (2) $\alpha_\parallel = \alpha_\perp = \alpha/\sqrt{2}$; the Rashba model is obtained after we rotate the spin by 90 degrees while leaving the momentum space unchanged [46].

The vector $\boldsymbol{g}(\boldsymbol{k})$, written in polar coordinates as

$$\boldsymbol{g}(\boldsymbol{k}) = |\boldsymbol{g}(\boldsymbol{k})| \cdot \hat{\boldsymbol{g}}(\boldsymbol{k}) \equiv \frac{\Delta(\boldsymbol{k})}{2}(\cos\Theta(\boldsymbol{k}), \sin\Theta(\boldsymbol{k})), \tag{3}$$

serves as an effective magnetic field in the momentum space. Spin-degenerated states are then lifted into two bands

$$\epsilon(\boldsymbol{k}, \pm) = \frac{\hbar^2 k^2}{2m} \pm \frac{\Delta(\boldsymbol{k})}{2}, \tag{4}$$

with band indices $\gamma = +, -$. The spin-splitting energy is accordingly $\Delta(\boldsymbol{k})$. The spin wave function for the state $(\boldsymbol{k}, \gamma)$ is expressed in the basis of eigenstates of spin σ_z as

$$|\boldsymbol{k}, +\rangle = \cos\frac{\Theta(\boldsymbol{k})}{2}|\boldsymbol{k}, \uparrow\rangle + \sin\frac{\Theta(\boldsymbol{k})}{2}|\boldsymbol{k}, \downarrow\rangle, \tag{5a}$$

$$|\boldsymbol{k}, -\rangle = \sin\frac{\Theta(\boldsymbol{k})}{2}|\boldsymbol{k}, \uparrow\rangle - \cos\frac{\Theta(\boldsymbol{k})}{2}|\boldsymbol{k}, \downarrow\rangle, \tag{5b}$$

which has spin polarization in $\boldsymbol{S}(\boldsymbol{k}, \gamma) \equiv \langle \boldsymbol{k}, \gamma|\boldsymbol{\sigma}|\boldsymbol{k}, \gamma\rangle = \gamma \cdot \hat{\boldsymbol{g}}(\boldsymbol{k})$. As a result, a hedgehog spin texture is formed on Fermi contours at Fermi energy $\epsilon_F = \epsilon(\boldsymbol{k}, \gamma) > 0$ [Fig. 1(d)]. The radii of the Fermi contours can be typically measured by $k_F \equiv \sqrt{2m\epsilon_F}/\hbar$, but are modulated for each band $\gamma = \pm$ and direction θ. In the highly anisotropic SOC case when $\delta \to 0$ or $\pi/2$, the whole spin texture tends to face in the same direction, and that component of spin becomes nearly conserved.

The BTE for the 2D electron system is given by

$$\frac{\partial f}{\partial t} + \boldsymbol{v} \cdot \frac{\partial f}{\partial \boldsymbol{r}} + \frac{(-e)\boldsymbol{E}}{\hbar} \cdot \frac{\partial f}{\partial \boldsymbol{k}} = \frac{df}{dt}\Big|_{\rm col}, \tag{6}$$

with charge of the electron $(-e)$ and group velocity $\boldsymbol{v} = \boldsymbol{v}(\boldsymbol{k}, \gamma) = \hbar^{-1}\nabla_{\boldsymbol{k}}\epsilon(\boldsymbol{k}, \gamma)$. Here the nonequilibrium distribution function $f = f(t, \boldsymbol{r}, \boldsymbol{k}, \gamma)$ is the number of electrons in a band γ occupying the volume of the phase space $d\boldsymbol{r}d\boldsymbol{k}$ at a time t. In equilibrium, it is identical to the Fermi distribution function $f = f_0(\epsilon(\boldsymbol{k}, \gamma))$. Here we assume that the system is in the low temperature $k_B T \ll \epsilon_F$. The chemical potential μ then satisfies $\mu \simeq \epsilon_F$.

The right-hand side of Eq. (6) is a collision integral for nonmagnetic impurity scattering. We assume that the impurity potential is like a δ function with strength v_0, randomly distributed with the density $n_{\rm imp}$ in the 2D system with the areal volume V. The collision integral is then derived along the Fermi golden rule (Sec. S2 of the Supplemental Material [27]) as

$$\frac{df}{dt}\Big|_{\rm col} = \frac{2\pi v_0^2 n_{\rm imp}}{\hbar V}\sum_{\boldsymbol{k}', \gamma'}|\langle \boldsymbol{k}', \gamma'|\boldsymbol{k}, \gamma\rangle|^2 \times [f(\boldsymbol{k}', \gamma') - f(\boldsymbol{k}, \gamma)] \cdot \delta(\epsilon(\boldsymbol{k}', \gamma') - \epsilon(\boldsymbol{k}, \gamma)). \tag{7}$$

The factor $|\langle \boldsymbol{k}', \gamma'|\boldsymbol{k}, \gamma\rangle|^2$, represented as

$$|\langle \boldsymbol{k}', \gamma'|\boldsymbol{k}, \gamma\rangle|^2 = \frac{1 + \boldsymbol{S}(\boldsymbol{k}, \gamma) \cdot \boldsymbol{S}(\boldsymbol{k}', \gamma')}{2}, \tag{8}$$

measures the relative angle of spin polarization between states before and after the spin-conserving scattering [47]. Spin relaxation and diffusion in this system are thus associated with the spin-dependent transition probability caused by the noncollinear spin texture in the momentum space. The collision integral (7) also indicates a typical impurity scattering rate, i.e., an inverse of quasiparticle lifetime

$$\frac{1}{\tau_p} \equiv \frac{2\pi v_0^2 n_{\rm imp} \cdot N_0/2}{\hbar}. \tag{9}$$

Here $N_0 = m/(\pi\hbar^2)$ is an exact density of states of this 2D system (Sec. S2 of the Supplemental Material [27]).

The validity of the BTE shown above for spin-splitting bands is supported by a derivation from the Keldysh Green's function method (Sec. S4 of the Supplemental Material [27]), which tells us that the BTE is valid in a clean limit $\hbar/\tau_p \ll \Delta_F \ll \epsilon_F$. Here $\Delta_F = \Delta(k_F)$ is the spin-splitting energy gap around the Fermi energy ϵ_F. This condition validates the BTEs for each band, which are coupled through the collision integral.

In addition to the BTE, we must consider the Gauss law, described as

$$\nabla \cdot \boldsymbol{E}(t, \boldsymbol{r}) = \frac{-e}{\varepsilon_0 d_y V}\sum_{\boldsymbol{k}, \gamma}[f(t, \boldsymbol{r}, \boldsymbol{k}, \gamma) - f_0(\epsilon(\boldsymbol{k}, \gamma))]. \tag{10}$$

Here we denote by d_y a typical length normal to the surface. The right-hand side stands for the charge density induced by the shift of the Fermi contours.

In the rest of Sec. II, we apply Eqs. (6)–(10) to the transport at the surface slightly out of equilibrium. We consider the following two cases in the absence of external fields in order to extract spin relaxation time and spin diffusion length: spatially uniform relaxation and temporary stationary diffusion. We also consider the linear response to a uniform stationary electric field in Sec. S3 of the Supplemental Material [27].

B. Spin relaxation time

When we consider the relaxation of a spatially uniform nonequilibrium state, the left-hand side of the BTE (6) is reduced to only a time-derivative term,

$$\frac{\partial f}{\partial t} = \frac{df}{dt}\Big|_{\rm col}. \tag{11}$$

We are interested in the relaxation of low-energy states. We thus assume that electron distribution $f = f(t, \boldsymbol{k}, \gamma)$ is displaced around the Fermi energy ϵ_F and seek for a solution to

Eq. (11) in the form

$$f(t,\boldsymbol{k},\gamma) = f_0(\epsilon(\boldsymbol{k},\gamma)) + e^{-t/\tau}\varphi_\tau(\boldsymbol{k},\gamma)\left(-\frac{\partial f_0(\epsilon)}{\partial\epsilon}\right), \quad (12)$$

with $-\partial_\epsilon f_0(\epsilon) \simeq \delta(\epsilon(\boldsymbol{k},\gamma) - \epsilon_\mathrm{F})$. The BTE after substitution of this assumption (12) results in an eigenvalue problem around the Fermi contours $\epsilon(\boldsymbol{k},\gamma) = \epsilon_\mathrm{F}$, written as

$$\lambda_\tau \varphi_\tau(\boldsymbol{k},\gamma) = \sum_{\boldsymbol{k}',\gamma'} M_\mathrm{col}(\boldsymbol{k},\gamma,\boldsymbol{k}',\gamma')\varphi_\tau(\boldsymbol{k}',\gamma'). \quad (13)$$

Here we defined eigenvalue $\lambda_\tau = -\tau_\mathrm{p}/\tau$ and a symmetric matrix between the states $(\boldsymbol{k},\gamma)$ and $(\boldsymbol{k}',\gamma')$

$$M_\mathrm{col}(\boldsymbol{k},\gamma,\boldsymbol{k}',\gamma') = \frac{1}{VN_0/2}\sum_{\boldsymbol{k}'',\gamma''} |\langle \boldsymbol{k}'',\gamma''|\boldsymbol{k},\gamma\rangle|^2 \times (\delta_{\boldsymbol{k}',\boldsymbol{k}''}\delta_{\gamma',\gamma''} - \delta_{\boldsymbol{k},\boldsymbol{k}'}\delta_{\gamma,\gamma'}) \cdot \delta(\epsilon(\boldsymbol{k}'',\gamma'') - \epsilon(\boldsymbol{k},\gamma)), \quad (14)$$

which we shall refer to as the *relaxation matrix* (this can be regarded as the integral kernel because the collision integral is an integral transform of the distribution function). Let $\tau(j)$ be the relaxation time of the jth eigenvector $\varphi_{\tau(j)}$ of Eq. (13). The general solution (restricted to the low-energy state) to Eq. (11) is given in the form

$$f(t,\boldsymbol{k},\gamma) = f_0(\epsilon(\boldsymbol{k},\gamma)) + \sum_j c(j)e^{-t/\tau(j)}\varphi_{\tau(j)}(\boldsymbol{k},\gamma) \times \left(-\frac{\partial f_0(\epsilon)}{\partial\epsilon}\right), \quad (15)$$

where the coefficients $c(j)$ are determined by the initial distribution function in a relaxation process. The μ $(= x, z)$ component of the spin density at time t is given by

$$\sum_{\boldsymbol{k},\gamma} \frac{\langle \boldsymbol{k},\gamma|\sigma_\mu|\boldsymbol{k},\gamma\rangle}{V} f(t,\boldsymbol{k},\gamma) = \langle s_\mu\rangle_\mathrm{eq} + \sum_j c(j)e^{-t/\tau(j)}s_\mu^\mathrm{relax}(j), \quad (16)$$

with

$$s_\mu^\mathrm{relax}(j) = \frac{1}{V}\sum_{\boldsymbol{k},\gamma}\langle \boldsymbol{k},\gamma|\sigma_\mu|\boldsymbol{k},\gamma\rangle\varphi_{\tau(j)}(\boldsymbol{k},\gamma)\left(-\frac{\partial f_0(\epsilon)}{\partial\epsilon}\right). \quad (17)$$

When $s_\mu^\mathrm{relax}(j) \neq 0$, we say that the jth eigenmode *carries* s_μ. We identify the longest relaxation time $\tau(j)$ among those of eigenmodes j carrying s_μ with the spin relaxation time for s_μ.

The eigenvalue spectrum τ_p/τ is plotted with varying anisotropy of the SOC δ in Fig. 2(a). Here one trivial mode $\varphi_\tau =$ constant with $\tau_\mathrm{p}/\tau = 0$ is omitted from the plots since it violates the charge neutrality condition (10) with $\boldsymbol{E} = 0$ [48], while the other eigenmodes automatically satisfy that condition (Sec. S3 of the Supplemental Material [27]). Most eigenvalues are located at $\tau = \tau_\mathrm{p}$ but two eigenmodes have relaxation times longer than the others. We will focus on the latter two modes.

We confirm that the mode with the relaxation time diverging as $\delta \to 0$ $(\delta \to \pi/2)$ carries the z (x) component of spin. It can be naturally understood from the fact that the

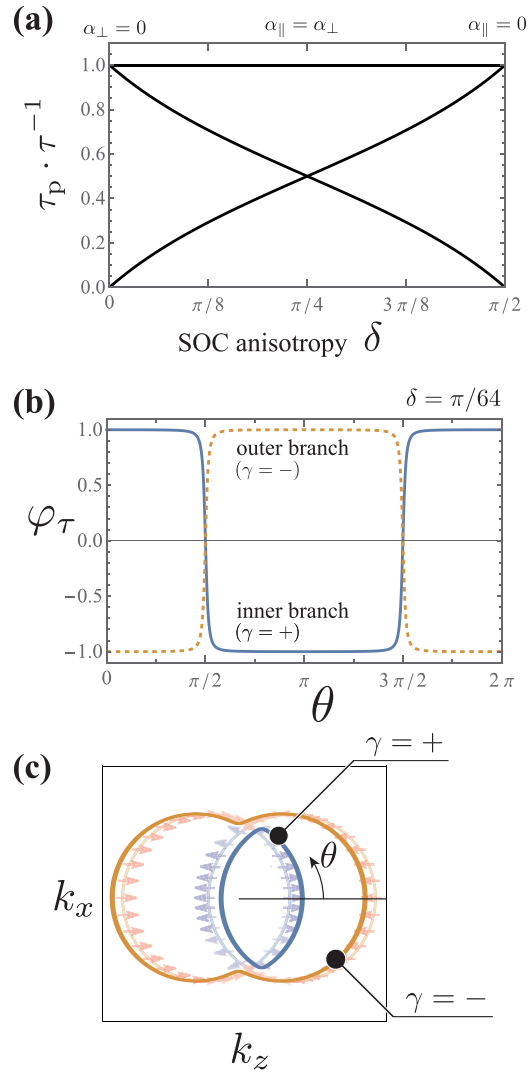

FIG. 2. Eigenmode analysis of the Boltzmann transport equation for relaxation. (a) Inverse of the relaxation time τ plotted for all modes and for various anisotropy $\alpha_\perp/\alpha_\parallel = \tan\delta$. All eigenmodes but two are degenerate in $\tau = \tau_\mathrm{p}$. (b) Deviation from equilibrium in the distribution function around the Fermi contours $\varphi_\tau(\theta,\gamma)$ that has the longest relaxation time when $\delta = \pi/64$. The amplitude is put in arbitrary units. (c) Schematic illustration of the deviation of the electron distribution (b), drawn as a shift of the Fermi contours.

spin component in the z (x) direction is conserved in the highly anisotropic limit $\delta \to 0$ $(\pi/2)$, i.e., $\alpha_\perp \to 0$ $(\alpha_\parallel \to 0)$. Figure 2(b) shows the deviation $\varphi_\tau(\boldsymbol{k},\gamma) = \varphi_\tau(\theta,\gamma)$ in distribution function of the slowest mode from the equilibrium, when spin s_z is almost conserved $(\alpha_\parallel \gg \alpha_\perp)$. The inner and outer Fermi contours are shifted in opposite directions, which induces nonzero spin density in the z direction, as shown in Fig. 2(c). Indeed, $\varphi_\tau(\boldsymbol{k},\gamma)$ is analytically expressed as $\varphi_\tau(\boldsymbol{k},\gamma) \propto \gamma\cos\Theta(\theta) = \langle \boldsymbol{k},\gamma|\sigma_z|\boldsymbol{k},\gamma\rangle$ (Sec. S3 of the Supplemental Material [27]). It follows that this slow mode φ_τ has nonzero $s_z^\mathrm{relax}(j)$ defined in Eq. (17), i.e., carries the z component of spin density, regardless of the anisotropy δ. We obtain the analytical expressions for the two spin relaxation times shown in Fig. 2(a), as a function of the anisotropy angle δ, and we find that they are independent of the SOC

strength α (the explicit expressions are available in Sec. S3). Such a characteristic spin relaxation time is attributed to the BTE scheme, which is valid in the clean limit or strong SOC case. In a region $\Delta_{\rm F}\tau_{\rm p}/\hbar \ll 1$ [49], on the other hand, the semiclassical picture of the spin-splitting bands breaks down. The spin relaxation time then follows the Elliott-Yafet [50,51] and D'yakonov-Perel' [52] mechanisms, instead of our description here.

C. Spin diffusion length

Spin diffusion length is extracted in the same way as the spin relaxation times, except for the treatment of the Gauss law. The spatially inhomogeneous charge distribution accompanied by the diffusion induces an internal electric field. The stationary diffusion thus follows both the BTE and Gauss law,

$$\boldsymbol{v}\cdot\frac{\partial f}{\partial \boldsymbol{r}}+\frac{(-e)\boldsymbol{E}_{\rm in}}{\hbar}\cdot\frac{\partial f}{\partial \boldsymbol{k}}=\left.\frac{df}{dt}\right|_{\rm col}, \tag{18a}$$

$$\nabla\cdot\boldsymbol{E}_{\rm in}=\frac{-e}{\varepsilon_0 d_y V}\sum_{\boldsymbol{k},\gamma}[f(\boldsymbol{r},\boldsymbol{k},\gamma)-f_0(\epsilon(\boldsymbol{k},\gamma))], \tag{18b}$$

where the internal electric field $\boldsymbol{E}_{\rm in}$ works for charge screening effect. We then assume that the distribution function $f(\boldsymbol{r},\boldsymbol{k},\gamma)$ and the electric field $\boldsymbol{E}_{\rm in}$ decay in the $+z$ direction with a diffusion length $\ell>0$, represented as

$$f(\boldsymbol{r},\boldsymbol{k},\gamma)=f_0(\epsilon(\boldsymbol{k},\gamma))+e^{-z/\ell}\varphi_\ell(\boldsymbol{k},\gamma)\left(-\frac{\partial f_0(\epsilon)}{\partial\epsilon}\right), \tag{19a}$$

$$E_{{\rm in},z}=\frac{\mathcal{E}_\ell}{(-e)v_{\rm F}\tau_{\rm p}}e^{-z/\ell}, \tag{19b}$$

with $v_{\rm F}=\hbar k_{\rm F}/m$ a typical Fermi velocity. Substitution of Eqs. (19) to Eqs. (18) yields a generalized eigenvalue problem with eigenvalues $-v_{\rm F}\tau_{\rm p}/\ell$ and eigenvectors $(\{\varphi_\ell(\boldsymbol{k},\gamma)\},\mathcal{E}_\ell)$ to be determined (Sec. S3 of the Supplemental Material [27]).

Similarly to the characterization of the relaxation eigenmode in the previous subsection, we say that the jth eigenmode of spatial decaying *carries* s_μ when $s_\mu^{\rm diff}(j)\neq 0$ with

$$s_\mu^{\rm diff}(j)=\frac{1}{V}\sum_{\boldsymbol{k},\gamma}\langle\boldsymbol{k},\gamma|\sigma_\mu|\boldsymbol{k},\gamma\rangle\varphi_{\ell(j)}(\boldsymbol{k},\gamma)\left(-\frac{\partial f_0(\epsilon)}{\partial\epsilon}\right). \tag{20}$$

We identify the longest decay length $\ell(j)$ among those of eigenmodes j carrying s_μ with the spin diffusion length for s_μ.

In solving this problem, we have to fix a dimensionless parameter, i.e., a ratio of charge screening length to diffusion length

$$\eta^{-1}\equiv(v_{\rm F}\tau_{\rm p})^2\cdot\left(\frac{e^2N_0/2}{\varepsilon_0 d_y}\right)\sim(v_{\rm F}\tau_{\rm p}q_{\rm TF})^2\sim 10^6, \tag{21}$$

with $v_{\rm F}\tau_{\rm p}\sim 10^{-8}$ m and Thomas-Fermi screening wave vector $q_{\rm TF}\sim 10^{11}$ m^{-1}. Numerical details of the dimensionless parameter η, however, give no striking difference in the results presented below.

The eigenvalue spectrum, which presents the inverse of the diffusion length of each mode, is plotted in Fig. 3(a). The spectrum is originally symmetric in $\pm\ell$ since diffusions in the $\pm z$ direction are equivalent. We plot here only positive diffusion length $\ell>0$. We also neglect a mode $v_{\rm F}\tau_{\rm p}/\ell=0$ since it describes homogeneous charge current density without external fields.

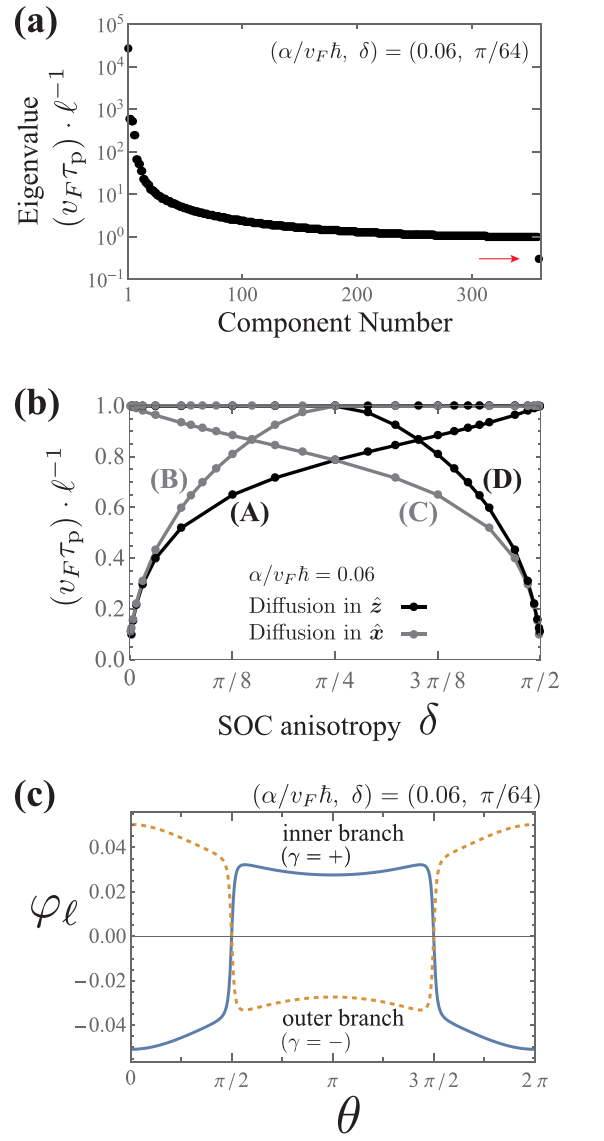

FIG. 3. Eigenmode analysis of Boltzmann transport equation for diffusion. (a) Eigenvalues corresponding to inverse of the diffusion length $\ell>0$ arranged in descending order. The red arrow points to an isolated slowly decaying mode. The total number of components reflects the 358 grids in the azimuthal direction around the Fermi contour used in the numerical calculation. (b) Inverse of the diffusion length ℓ plotted for the isolated slowly decaying modes labeled (A)–(D) and for different anisotropy δ. Both diffusion lengths in the z direction and that in the x direction are shown. (c) Deviation from equilibrium in distribution function around the Fermi contours $\varphi_\ell(\theta,\gamma)$ that has the longest diffusion length when diffusing in the z direction. The amplitude is put in arbitrary units.

Most positive eigenvalues are continuously distributed and are concentrated around $\ell=v_{\rm F}\tau_{\rm p}$. There exist, however, isolated modes that have longer diffusion length than the others.

Figure 3(b) shows the inverse of such long diffusion lengths plotted for different anisotropy of the SOC. The same figure also shows the result for the case when the x direction

is substituted for the z direction in Eq. (19). We confirm that each of the slowly decaying modes (A)–(D) as spin diffusion carries a different spin component into a different direction. As for the diffusion in the $+z$ direction [branches (A) or (D)], the diffusion length diverges at $\delta \to 0$ or $\pi/2$, which results from good conservation of spin s_z or s_x, respectively. It follows that branch (A) carries spin s_z, while (D) carries spin s_x in the $+z$ direction. That is supported by spin density calculation based on the shift of the Fermi contours [Fig. 3(c) depicts the branch (A)]. In the same manner, the branches (B), (C) are characterized as spin s_z, s_x diffusion in the $+x$ direction, respectively. Spin diffusion length for each spin component and each diffusion direction is thus uniquely defined as the diffusion length of corresponding slowly decaying modes (A)–(D).

III. CHARGE-SPIN INTERCONVERSION AT THE INTERFACE

A. Formulation for the interface

We turn to the Edelstein effect (EE) and the inverse Edelstein effect (IEE) at the 2D surface of the chiral metal attached with a 3D nonmagnetic metal. The presence of an interface is treated as a boundary condition for the electron distribution in the 3D metal [see Figs. 1(b) and 1(c)], while it introduces an additional relaxation matrix and a driving term to the 2D system we have examined. We now apply the electric field $\boldsymbol{E}$ in the z direction on the surface [Fig. 1(b)], or inject spins with polarization in the z direction [Fig. 1(c)], both of which favor the z component of spin polarization in the 3D metal. More generally, spin polarization of the 3D metal can point in an arbitrary direction, and we consider such cases in Secs. S5 and S7 of the Supplemental Material [27]. In the following, we assume that both the 2D and attached 3D metals are electrically neutral and have a common chemical potential μ_0, for simplicity.

We first explain the 3D nonmagnetic metal. As illustrated in Figs. 1(b) and 1(c), it is placed at $0 \leqslant y \leqslant L$ with the $y = 0$ plane the interface at the chiral metal and the $y = L$ plane an open end or interface with spin current source. In the bulk, the one-particle state is specified by wave vector $\boldsymbol{q}$ and z component of spin σ, denoted as $|\boldsymbol{q}, \sigma\rangle$. The energy $\epsilon^{(\mathrm{n})}(|\boldsymbol{q}|)$ of that state is degenerate with spin degrees of freedom and isotropic as a function of the modulus of $\boldsymbol{q}$. We denote the distribution function in the 3D nonmagnetic metal as $F(t, \boldsymbol{r}, \boldsymbol{q}, \sigma)$.

To describe the effect of the interface, we adopt a tunneling Hamiltonian

$$\hat{H}_{\mathrm{T}} = \sum_{\boldsymbol{k},\boldsymbol{q}} \sum_{\sigma=\uparrow,\downarrow} [T_{\boldsymbol{kq}} \, |\boldsymbol{k}, \sigma\rangle \, (\boldsymbol{q}, \sigma| + T^*_{\boldsymbol{kq}} |\boldsymbol{q}, \sigma) \, \langle \boldsymbol{k}, \sigma|], \quad (22)$$

which allows spin-independent transmission across the interface. Here we consider that the interface between the two metals is rough enough to randomize momentum. That enables us to take $T_{\boldsymbol{kq}} = T$. The net transition rates into $|\boldsymbol{k}, \gamma\rangle$ and $|\boldsymbol{q}, \sigma)$ are, respectively, given by the Fermi golden rule as

$$\left.\frac{df(t, \boldsymbol{r}, \boldsymbol{k}, \gamma)}{dt}\right|_{\mathrm{int}} = \frac{2\pi |T|^2}{\hbar} \sum_{\boldsymbol{q},\sigma} |\, \langle \boldsymbol{k}, \gamma | \sigma \rangle \,|^2 \times [F(t, \boldsymbol{r}, \boldsymbol{q}, \sigma) - f(t, \boldsymbol{r}, \boldsymbol{k}, \gamma) \times \delta(\epsilon(\boldsymbol{k}, \gamma) - \epsilon^{(\mathrm{n})}(\boldsymbol{q})) \quad (23a)$$

and

$$\left.\frac{dF(t, \boldsymbol{r}, \boldsymbol{q}, \sigma)}{dt}\right|_{\mathrm{int}} = \frac{2\pi |T|^2}{\hbar} \sum_{\boldsymbol{k},\gamma} |\, \langle \boldsymbol{k}, \gamma | \sigma \rangle \,|^2 \times [f(t, \boldsymbol{r}, \boldsymbol{k}, \gamma) - F(t, \boldsymbol{r}, \boldsymbol{q}, \sigma)] \times \delta(\epsilon(\boldsymbol{k}, \gamma) - \epsilon^{(\mathrm{n})}(\boldsymbol{q})), \quad (23b)$$

with $\boldsymbol{r}$ in the $y = 0$ plane. These terms serve as extra collision terms in the BTE in the 2D and 3D metals. They vanish in equilibrium, and we can replace f and F in Eqs. (23) by the deviation from the equilibrium

$$f(t, \boldsymbol{r}, \boldsymbol{k}, \gamma) - f_0(\epsilon(\boldsymbol{k}, \gamma)) = -\frac{\partial f_0(\epsilon(\boldsymbol{k}, \gamma))}{\partial \epsilon(\boldsymbol{k}, \gamma)} \varphi(t, \boldsymbol{r}, \boldsymbol{k}, \gamma) \quad (24)$$

and $F_1(t, \boldsymbol{r}, \boldsymbol{q}, \sigma) = F(t, \boldsymbol{r}, \boldsymbol{q}, \sigma) - f_0(\epsilon^{(\mathrm{n})}(|\boldsymbol{q}|))$. In the following, we consider that the whole system is stationary and spatially homogeneous in the z and x directions, parallel to the interface [see Fig. 1(a), where the x, y, z directions are shown]. We also denote the transmission rate across the interface [9] by

$$\frac{1}{\tau_{\mathrm{t}}} \equiv \frac{2\pi |T|^2 V^{(\mathrm{n})} N^{(\mathrm{n})}(\mu_0)/2}{\hbar}. \quad (25)$$

Here $N^{(\mathrm{n})}(\epsilon) = 2(V^{(\mathrm{n})})^{-1} \sum_{\boldsymbol{q}} \delta(\epsilon - \epsilon^{(\mathrm{n})}(\boldsymbol{q}))$ is the density of states per volume of the 3D system $V^{(\mathrm{n})}$.

Let us write down the electron distribution in the 3D metal. We assume that both the spin-conserving impurity scattering and much weaker spin-flip impurity scattering occur in the 3D metal. The BTE in that nonmagnetic metal is examined by Valet and Fert [26], and is briefly reviewed in Sec. S6 of the Supplemental Material [27]. In the absence of external fields, the shift of the distribution F_1 they provide is expressed as

$$F_1(y, \boldsymbol{q}, \sigma) = -\frac{\partial f_0(\epsilon^{(\mathrm{n})}(|\boldsymbol{q}|))}{\partial \epsilon} \{\bar{\mu} - \mu_0 + \frac{\sigma}{2} \left[\mu_{\mathrm{s}}^{(\mathrm{n})}(y) + \frac{2e^2 \lambda^{(\mathrm{n})}}{\sigma^{(\mathrm{n})}} \frac{q_y}{|\boldsymbol{q}|} J_{\mathrm{s}}^{(\mathrm{n})}(y) \right] \} \quad (26)$$

and higher multipole terms in $\boldsymbol{q}$ proportional to the Legendre polynomials $P_m(q_y/|\boldsymbol{q}|)$ with $m \geqslant 2$, which are negligibly small. Here $\lambda^{(\mathrm{n})}$ and $\sigma^{(\mathrm{n})}$ are the electron mean free path and the electrical conductivity summed over spins, respectively, while $\bar{\mu}$ is a constant to be determined later. The two spatially varying quantities

$$\mu_{\mathrm{s}}^{(\mathrm{n})}(y) = 2(Ae^{-y/\ell_{\mathrm{sf}}} + Be^{y/\ell_{\mathrm{sf}}}), \quad (27a)$$

$$J_{\mathrm{s}}^{(\mathrm{n})}(y) = \frac{\sigma^{(\mathrm{n})}}{e^2 \ell_{\mathrm{sf}}} (Ae^{-y/\ell_{\mathrm{sf}}} - Be^{y/\ell_{\mathrm{sf}}}) \quad (27b)$$

are spin accumulation polarized in the z direction and spin current density flowing parallel to the y direction, respectively. They follow the spin diffusion equation with spin diffusion length ℓ_{sf} [26], but two coefficients A, B in them are still undetermined. For later use, we here introduce a dimensionless parameter $\tau_{\mathrm{p}}/\tau_{\mathrm{3D}}$ that measures spin diffusion in the 3D metal with a typical rate

$$\frac{1}{\tau_{\mathrm{3D}}} \equiv \frac{\sigma^{(\mathrm{n})}}{e^2 \ell_{\mathrm{sf}} N_0}. \quad (28)$$

When the spin-flip scattering relaxation time $\tau_{\rm sf}$ is much longer than the spin-conserving scattering relaxation time $\tau_{\rm s}$, this timescale $\tau_{\rm 3D}$ is given as $\tau_{\rm 3D} \simeq N_0 \cdot [N^{(\rm n)}(\mu_0) v_{\rm F}^{(\rm n)}]^{-1} \cdot \sqrt{3\tau_{\rm sf}/(2\tau_{\rm s})}$ with the Fermi velocity in the 3D metal $v_{\rm F}^{(\rm n)}$ (Sec. S7 of the Supplemental Material [27]).

To determine the electron distribution (26) with (27) described by Valet and Fert, we consider boundary conditions to the 3D metal based on the extra collision term (23b) at the interface. There are three conditions: (i) the absence of charge current through the interface, (ii) the continuity of spin current at the interface, and (iii) the boundary condition on the other side of the 3D metal at $y = L$. The three parameters $\bar{\mu}$, A, and B will be then expressed as the functionals of the distribution function in the 2D metal.

The first condition (i) is described as

$$\frac{1}{V}\sum_{\boldsymbol{q},\sigma} \left.\frac{dF(y=0,\boldsymbol{q},\sigma)}{dt}\right|_{\rm int} = 0, \tag{29}$$

with the left-hand side being the number of electrons flowing through the unit area of the interface from the 2D metal to the 3D metal per unit time. This condition yields the balance of electrochemical potentials on both sides of the interface

$$\bar{\mu} - \mu_0 = \frac{1}{VN_0}\sum_{\boldsymbol{k},\gamma} \varphi(\boldsymbol{k},\gamma)\delta(\epsilon(\boldsymbol{k},\gamma) - \mu_0), \tag{30}$$

with the right-hand side net charge density of the 2D metal divided by $-e$ times the density of states. As we have first assumed that the whole system is electrically neutral with the same chemical potential μ_0, both sides of Eq. (30) are zero; it follows that $\bar{\mu} = \mu_0$ and the charge neutrality condition for the 2D system.

We turn to the remaining conditions. The condition (ii) on the transmission of the z-component spin is described in the same way as Eq. (29),

$$\frac{1}{V}\sum_{\boldsymbol{q},\sigma} \sigma \left.\frac{dF(y=0,\boldsymbol{q},\sigma)}{dt}\right|_{\rm int} = J_{\rm s}^{(\rm n)}(y=+0), \tag{31}$$

with the right-hand side given by Eq. (27b). As for the condition (iii), we assume either that the 3D metal has an open end at $y = L$ or that the 3D metal is attached with the source of spin current—such as a ferromagnetic metal or a metal with strong spin Hall effect at this location $y = L$. In both cases, the boundary condition is expressed as

$$J_{\rm s}^{(\rm n)}(y=L) = 0 \text{ or } J_{\rm s}^{\rm ext}, \tag{32}$$

where $J_{\rm s}^{\rm ext} \neq 0$ implies the external spin current injected from the source. The relations (31) and (32) determine the parameters A and B (Sec. S7 of the Supplemental Material [27]).

The Valet-Fert solution $F(y,\boldsymbol{q},\sigma)$ is thus determined by the distribution function $\varphi(\boldsymbol{k},\gamma)$ in the 2D metal and the spin current density at the boundary $J_{\rm s}^{(\rm n)}(L)$. It follows that the electron in the 2D metal under an electric field is described by

$$(-e)E v_z(\boldsymbol{k},\gamma)\frac{\partial f_0(\boldsymbol{k},\gamma)}{\partial\epsilon(\boldsymbol{k},\gamma)} = \left.\frac{df}{dt}\right|_{\rm col} + \left.\frac{df}{dt}\right|_{\rm int}, \tag{33}$$

with the second term on the right-hand side the extra Boltzmann collision term (23a), which is written with φ and $J_{\rm s}^{(\rm n)}(L)$. This extra term also includes three dimensionless parameters $L/\ell_{\rm sf}$, $\tau_{\rm p}/\tau_{\rm t}$, and $\tau_{\rm p}/\tau_{\rm 3D}$, which provide information on the 3D metal and the interface. The effective BTE (33) for 2D electron distribution is simplified as

$$b_{\rm EE}(\boldsymbol{k},\gamma) + b_{\rm IEE}(\boldsymbol{k},\gamma) = \sum_{\boldsymbol{k}',\gamma'} M_{\rm tot}(\boldsymbol{k},\gamma,\boldsymbol{k}',\gamma')\varphi(\boldsymbol{k}',\gamma') \tag{34}$$

for $|\boldsymbol{k},\gamma\rangle$ such that $\epsilon(\boldsymbol{k},\gamma) = \mu_0$ (Sec. S7 of the Supplemental Material [27]). The two terms on the left-hand side are driving forces: One term is the electric field applied on the surface

$$b_{\rm EE}(\boldsymbol{k},\gamma) \equiv eE\tau_{\rm p} v_z(\boldsymbol{k},\gamma), \tag{35a}$$

which is a source of the EE—charge-to-spin conversion. The other term is the spin current injected from the 3D metal

$$b_{\rm IEE}(\boldsymbol{k},\gamma) \equiv \frac{2K\tau_{\rm p} J_{\rm s}^{\rm ext}}{N_0}\cdot S_z(\boldsymbol{k},\gamma), \tag{35b}$$

which leads to the IEE—spin-to-charge conversion. Here we introduce a notation

$$2K \equiv [\cosh L/\ell_{\rm sf} + (\tau_{\rm t}/\tau_{\rm 3D})\sinh L/\ell_{\rm sf}]^{-1}. \tag{36}$$

The IEE source term (35b) indicates that the injected spin current serves as a time-dependent magnetic field coupling to the spin $S_z(\boldsymbol{k},\gamma) \equiv \langle\boldsymbol{k},\gamma|\sigma_z|\boldsymbol{k},\gamma\rangle$, inducing the nonequilibrium state in the surface [5,6].

On the right-hand side of Eq. (34), the relaxation matrix is given by two contributions $M_{\rm tot} = M_{\rm col} + M_{\rm int}$ where the matrix $M_{\rm col}$, provided in Eq. (14), stems from the impurity scattering within the surface, while

$$M_{\rm int}(\boldsymbol{k},\gamma,\boldsymbol{k}',\gamma') \equiv \frac{\tau_{\rm p}}{\tau_{\rm t}}\Big\{ -\delta_{\boldsymbol{k},\boldsymbol{k}'}\delta_{\gamma,\gamma'} + \frac{\delta(\epsilon(\boldsymbol{k},\gamma) - \epsilon(\boldsymbol{k}',\gamma'))}{N_0 V} \times [1 + K'\boldsymbol{S}(\boldsymbol{k},\gamma)\cdot\boldsymbol{S}(\boldsymbol{k}',\gamma')]\Big\}, \tag{37}$$

with $K' \equiv 2K\cosh L/\ell_{\rm sf}$ represents an effective scattering process mediated by the interface.

We here assume that no charge current is induced in the 3D metal without considering the penetration of an electric field applied on the 2D system into the 3D metal. Such leakage of the electric field in the EE case is small only when the 3D metal has low conductivity and/or the thickness L of the 3D metal is sufficiently small. It is thus generally needed to incorporate the charge current density in the 3D metal. We, however, restrict ourselves to neglecting that effect as a starting point of the formulation of the EE.

B. Comparison between the Edelstein effect and its inverse

Let us compare the nonequilibrium distributions of the EE and the IEE. In both effects, there exist charge current density and spin density induced in the 2D metal and spin accumulation and spin current density in the 3D metal. The deviations of the electron distribution around the Fermi contours $\varphi(\boldsymbol{k},\gamma) = \varphi(\theta,\gamma)$ for the two effects are, however, different, as can be seen from Figs. 4(a) and 4(b). Their analytical expressions are available in Sec. S8 of the Supplemental Material [27]. In the EE, $\varphi = \varphi_{\rm EE}(\theta,\gamma)$ driven by the external electric field $E \neq 0$ without spin current injection $J_{\rm s}^{(\rm n)}(L) = 0$ is illustrated in Fig. 4(a). The Fermi contours are basically

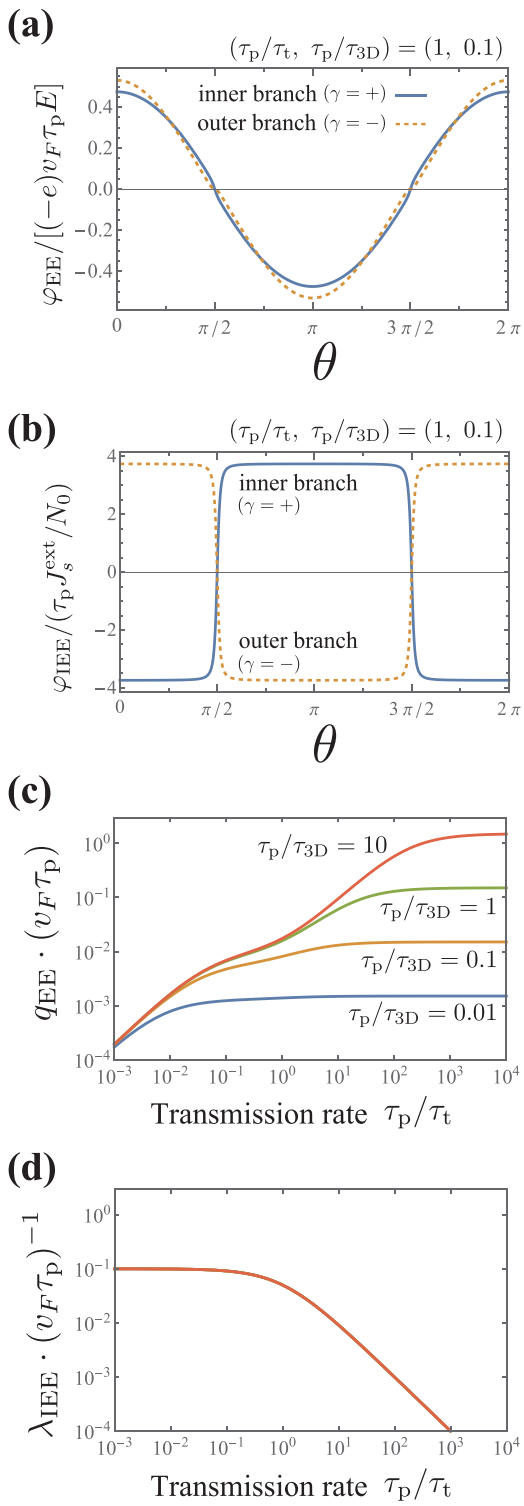

FIG. 4. The deviation from the equilibrium distribution function around the two Fermi contours for direct Edelstein effect [(a)] and inverse Edelstein effect [(b)], and associated charge-spin conversion efficiencies at the interface q_{EE} [(c)] and λ_{IEE} [(d)]. The parameters are chosen as $(\alpha/v_F\hbar, \delta, L/\ell_{sf}) = (0.1, \pi/64, 1)$. [(c), (d)] The colored lines show different spin diffusion rates in the three-dimensional nonmagnetic metal [defined in Eq. (28)]. Those lines collapse onto a single curve in (d).

shifted in the direction of the electric field with a relaxation time $(1/\tau_p + 1/\tau_t)^{-1}$, modified from the ordinary momentum relaxation time τ_p due to the interface transmission. More precisely, the deviation from the equilibrium distribution function for the two bands differ of order $\alpha/v_F\hbar$, which induces net spin density. In the IEE, on the other hand, the distribution function $\varphi = \varphi_{IEE}(\boldsymbol{k}, \gamma)$ driven by the external spin current $J_s^{(n)}(L) = J_s^{ext}$ without electric field $E = 0$ is illustrated in Fig. 4(b). The deviation changes its sign with respect to the band $\gamma = \pm$. Indeed, it is found analytically that the deviation is proportional to the spin polarization $S_z(\boldsymbol{k}, \gamma)$, which is the same as the spin s_z relaxation mode [Fig. 2(b)]. The different distribution functions given in Figs. 4(a) and 4(b) show that the EE and IEE are in different nonequilibrium states.

Linear responses found in the EE and IEE are different, consequently. We now consider charge-spin conversion efficiency—the ratio between electric current density in the 2D metal and spin current density in the 3D metal at the interface [8–10,12,14,40]. In the EE and IEE, that efficiency is defined as

$$q_{EE} \equiv \left.\frac{|J_s^{(n)}(y=0)|}{|j_c/(-e)|}\right|_{EE}, \tag{38a}$$

$$\lambda_{IEE} \equiv \left.\frac{|j_c/(-e)|}{|J_s^{(n)}(y=0)|}\right|_{IEE}, \tag{38b}$$

with $j_c = j_z^c$ a charge current density in the surface of the chiral metal, flowing in the z direction. The two efficiencies look similar but behave differently with respect to both the interface transmission rate $1/\tau_t$ and the detail of the 3D metal, specified by the timescale of spin diffusion τ_{3D} and the thickness L/ℓ_{sf}. Figure 4(c) shows that the charge current–to–spin current conversion efficiency q_{EE} decreases with τ_{3D}, while Fig. 4(d) shows that the spin current–to–charge current conversion efficiency λ_{IEE} is independent of τ_{3D}. It is also found that q_{EE} increases with the thickness of the 3D metal L/ℓ_{sf}, while λ_{IEE} is independent of L/ℓ_{sf} (Sec. S9 of the Supplemental Material [27]).

The efficiency λ_{IEE} is determined only by the interface—the nonequilibrium state in the 2D metal for the IEE case is affected only by the spin current injected from the interface $J_s^{(n)}(y=0)$. This explains why the details of the 3D metal do not affect the conversion efficiency λ_{IEE}. Indeed, λ_{IEE} is proportional to the modified relaxation time in the 2D metal by the interface transmission $(1/\tau_p + 1/\tau_t)^{-1}$ [9]. The increase of tunneling rate $1/\tau_t$ thus suppresses λ_{IEE}, as shown in Fig. 4(d).

The behavior of q_{EE}, on the other hand, depends on the details of the 3D metal; the timescale $\tau_{3D} \propto (\tau_{sf}/\tau_s)^{1/2}$ [see Eq. (28) for definition of τ_{3D}] increases and the thickness measured in units of the spin diffusion length L/ℓ_{sf} decreases when the spin-flip scattering is negligibly small, i.e., $\tau_{sf},\ \ell_{sf} \to \infty$. Stationary spin current density in the 3D metal, which is nearly constant in that case, is then suppressed since we impose the boundary condition $J_s^{(n)}(L) = 0$ for the EE case. The efficiency into spin current q_{EE} thus decreases with τ_{3D} but increases with L/ℓ_{sf}. Indeed, we find based on an

TABLE I. Comparison between previous studies and the present study with respect to the charge current–spin current conversion efficiency at the interface for the EE and IEE. "TI" stands for topological insulator. The definition of the efficiencies $q_{\rm EE}$ and $\lambda_{\rm IEE}$ are given in Eqs. (38).

	Zhang and Fert [8]	Dey *et al.* [9]	Isshiki *et al.* [40]	The present study ($\delta=\pi/4$, $L/\ell_{\rm sf}\to\infty$)
Subject	TI surface	TI surface	Rashba model	Chiral metal surface
$q_{\rm EE}$	$\dfrac{1}{v_{\rm F}(\tau_{\rm t}+\tau_{\rm sf})}$ [a]		$\dfrac{\alpha_{\rm R}}{v_{\rm F}\hbar}\cdot\dfrac{1}{v_{\rm F}\tau_{\rm t}}$ [b]	$\dfrac{\alpha/\sqrt{2}}{v_{\rm F}\hbar}\cdot\dfrac{2+O((\alpha/v_{\rm F}\hbar)^2)}{v_{\rm F}[\tau_{\rm t}+\tau_{\rm 3D}+(1/\tau_{\rm p}+1/\tau_{\rm t})^{-1}]}$
$\lambda_{\rm IEE}$	$v_{\rm F}\tau_{\rm p}$ [a]	$\dfrac{v_{\rm F}}{1/\tau_{\rm p}+2/\tau_{\rm t}}$ [c]	$\dfrac{\alpha_{\rm R}}{v_{\rm F}\hbar}\cdot\dfrac{v_{\rm F}}{1/\tau_{\rm p}+1/\tau_{\rm t}}$ [b]	$\dfrac{\alpha/\sqrt{2}}{v_{\rm F}\hbar}\cdot\dfrac{v_{\rm F}}{1/\tau_{\rm p}+1/\tau_{\rm t}}$

[a]Equations (13) and (19) in Ref. [8].
[b]Equations (3), (6), and (7) in Ref. [40].
[c]Equations (18) in Ref. [9].

analytical calculation that $q_{\rm EE}$ is roughly proportional to a rate $(\tau_{\rm t}+\tau_{\rm 3D}\coth L/\ell_{\rm sf})^{-1}$, which indicates the spin transmission rate across the interface into the 3D metal with finite thickness.

We now compare our results with previous studies, as summarized in Table I. Here the Rashba SOC $\alpha_{\rm R}(k_z\sigma_x-k_x\sigma_z)$ can be regarded as the isotropic case of the SOC here (2) with the Rashba parameter $\alpha_{\rm R}=\alpha/\sqrt{2}$, as we stated at the beginning of Sec. II A. The different behaviors between $q_{\rm EE}$ and $\lambda_{\rm IEE}$ were discussed by Zhang and Fert [8], where they considered charge-spin interconversion at the topological insulator surfaces. Dey *et al.* [9] then found that the efficiency $\lambda_{\rm IEE}$ is suppressed by the interface transmission rate $1/\tau_{\rm t}$, which is in good agreement with our results, except for the difference in the factor $(\alpha/\sqrt{2})/v_{\rm F}\hbar$ due to the difference in the targeted systems; indeed, $\tau_{\rm t}/2$ in their paper is equivalent to $\tau_{\rm t}$ in our study. Isshiki *et al.* [40] also provided phenomenological calculation of $q_{\rm EE}$ and $\lambda_{\rm IEE}$. Our analytical calculation practically supports their expression for $\lambda_{\rm IEE}$. A trade-off relation between the conversion efficiencies for the EE and IEE, proposed by Isshiki *et al.* [40], is also found in general, which is expressed as

$$q_{\rm EE}\cdot\lambda_{\rm IEE}<\frac{2\alpha_\parallel\alpha_\perp}{(v_{\rm F}\hbar)^2}. \tag{39}$$

The efficiency $q_{\rm EE}$ itself is, on the other hand, obtained on the basis of the Boltzmann equation by the present study. Indeed, $q_{\rm EE}$ obtained by Zhang and Fert [8] is similar to our result in that $\tau_{\rm 3D}\propto(\tau_{\rm sf}/\tau_{\rm s})^{1/2}$ consists of spin-flip scattering relaxation time. We, moreover, clarify the dependence of $q_{\rm EE}$ on the momentum relaxation time $\tau_{\rm p}$, the thickness $L/\ell_{\rm sf}$ (in Table I, we put it infinite), and the SOC anisotropy of the surface δ (in Table I, $\delta=\pi/4$). It also should be noted that the previous studies considered the spin accumulation at the interface as an external parameter in the formulation of both the EE and IEE. According to the experiments on the IEE [10,12,14], and on the chiral metals [15,17,18], however, the controllable parameter—which we can exert directly—to the 3D nonmagnetic metal is often spin current, injected or fixed to be zero at the open surface ($y=L$ plane in this study). We here adopt a formulation close to these experimental situations.

TABLE II. Ratios between physical quantities in the case of direct Edelstein effect, $\frac{Y}{X}|_{\rm EE}$, including the linear response to the electric field. The entry in the row X and column Y gives the ratio Y/X. The timescales $\tau_{\rm p}$ and $\tau_{\rm 3D}$ are defined in Eq. (9) and Eq. (28), respectively, while $\tau_{\rm a}$, $\tau_{\rm b}$, $\tilde{\alpha}$, and r are defined in Eqs. (40).

		Y				
		$2s_z/N_0$	$j_c/[(-e)v_{\rm F}N_0/2]$	$\mu_{\rm s}^{(n)}(0)$	$\mu_{\rm s}^{(n)}(L)$	$\tau_{\rm p}J_{\rm s}^{(n)}(0)/N_0$
X	$(-e)v_{\rm F}\tau_{\rm p}E$	$-2\tilde{\alpha}\sin\delta\cdot\dfrac{1/\tau_{\rm p}}{1/\tau_{\rm a}+1/\tau_{\rm b}}$ $=\dfrac{2}{N_0}\cdot\dfrac{\langle S_z,\,v_z\rangle}{v_{\rm F}}$	$\dfrac{(\tau_{\rm a}\tan\delta)\cdot r}{\tau_{\rm p}}$ $=\dfrac{2}{N_0}\cdot\dfrac{\langle v_z,\,v_z\rangle}{v_{\rm F}^2}$	$-2\tilde{\alpha}\sin\delta\cdot\dfrac{(\tau_{\rm 3D}/\tau_{\rm p})\coth L/\ell_{\rm sf}}{1+\tau_{\rm b}/\tau_{\rm a}}$	$\dfrac{-2\tilde{\alpha}\sin\delta(\tau_{\rm 3D}/\tau_{\rm p})}{(1+\tau_{\rm b}/\tau_{\rm a})\sinh L/\ell_{\rm sf}}$ $=-2\cdot\dfrac{\lambda_{\rm recip}}{v_{\rm F}\tau_{\rm p}}$	$\dfrac{-\tilde{\alpha}\sin\delta}{1+\tau_{\rm b}/\tau_{\rm a}}$
	$2s_z/N_0$	1	$-\dfrac{(1+\tau_{\rm a}/\tau_{\rm b})r}{2\tilde{\alpha}\cos\delta}$	$\dfrac{\tau_{\rm 3D}}{\tau_{\rm b}}\coth L/\ell_{\rm sf}$	$\dfrac{\tau_{\rm 3D}/\tau_{\rm b}}{\sinh L/\ell_{\rm sf}}$	$\dfrac{\tau_{\rm p}}{2\tau_{\rm b}}$
	$j_c/[(-e)v_{\rm F}N_0/2]$		1	$\dfrac{-2\tilde{\alpha}\cos\delta}{r}\cdot\dfrac{\tau_{\rm 3D}\coth L/\ell_{\rm sf}}{\tau_{\rm a}+\tau_{\rm b}}$	$\dfrac{-2\tilde{\alpha}\cos\delta}{r\sinh L/\ell_{\rm sf}}\cdot\dfrac{\tau_{\rm 3D}}{\tau_{\rm a}+\tau_{\rm b}}$	$\dfrac{-\tilde{\alpha}\cos\delta}{r}\cdot\dfrac{\tau_{\rm p}}{\tau_{\rm a}+\tau_{\rm b}}$ $=-q_{\rm EE}\cdot\dfrac{v_{\rm F}\tau_{\rm p}}{2}$
	$\mu_{\rm s}^{(n)}(0)$			1	$\dfrac{1}{\cosh L/\ell_{\rm sf}}$	$\dfrac{\tau_{\rm p}}{2\tau_{\rm 3D}\coth L/\ell_{\rm sf}}$
	$\mu_{\rm s}^{(n)}(L)$				1	$\dfrac{\tau_{\rm p}\sinh L/\ell_{\rm sf}}{2\tau_{\rm 3D}}$
	$\tau_{\rm p}J_{\rm s}^{(n)}(0)/N_0$					1

TABLE III. Ratios between physical quantities in the case of inverse Edelstein effect, $\frac{Y}{X}|_{\mathrm{IEE}}$. The entry in the row X and column Y gives the ratio Y/X. The timescales τ_{p}, τ_{t}, and τ_{3D} are defined in Eq. (9), Eq. (25), and Eq. (28), respectively, while τ_{a}, τ_{b}, τ_{c}, $\tilde{\alpha}$, and r are defined in Eqs. (40).

		Y				
		$2s_z/N_0$	$j_c/[(-e)v_{\mathrm{F}}N_0/2]$	$\mu_{\mathrm{s}}^{(n)}(0)$	$\mu_{\mathrm{s}}^{(n)}(L)$	$\tau_{\mathrm{p}}J_{\mathrm{s}}^{(n)}(0)/N_0$
X	$2s_z/N_0$	1				
	$j_c/[(-e)v_{\mathrm{F}}N_0/2]$	$\frac{-1}{\tilde{\alpha}\sin\delta}$	1			
	$\mu_{\mathrm{s}}^{(n)}(0)$	$\frac{1}{1+\tau_{\mathrm{t}}/\tau_{\mathrm{a}}}$	$\frac{-\tilde{\alpha}\sin\delta}{1+\tau_{\mathrm{t}}/\tau_{\mathrm{a}}} = \frac{1}{Q_{12}v_{\mathrm{F}}N_0}$	1		
	$\mu_{\mathrm{s}}^{(n)}(L)$	$\frac{\tau_{\mathrm{a}}}{\tau_{\mathrm{c}}\sinh L/\ell_{\mathrm{sf}}}$	$\frac{-\tilde{\alpha}\sin\delta\cdot\tau_{\mathrm{a}}}{\tau_{\mathrm{c}}\sinh L/\ell_{\mathrm{sf}}}$	$\frac{\tau_{\mathrm{t}}+\tau_{\mathrm{a}}}{\tau_{\mathrm{c}}\sinh L/\ell_{\mathrm{sf}}}$	1	
	$\tau_{\mathrm{p}}J_{\mathrm{s}}^{(n)}(0)/N_0$	$\frac{-2\tau_{\mathrm{a}}}{\tau_{\mathrm{p}}}$	$2\tilde{\alpha}\sin\delta\cdot\frac{\tau_{\mathrm{a}}}{\tau_{\mathrm{p}}} = 2\cdot\frac{\lambda_{\mathrm{IEE}}}{v_{\mathrm{F}}\tau_{\mathrm{p}}}$	$(-2)\cdot\frac{\tau_{\mathrm{t}}+\tau_{\mathrm{a}}}{\tau_{\mathrm{p}}}$	$\frac{-2\tau_{\mathrm{c}}}{\tau_{\mathrm{p}}}\cdot\sinh L/\ell_{\mathrm{sf}}$	1
	$\tau_{\mathrm{p}}J_{\mathrm{s}}^{(n)}(L)/N_0$	$\frac{-2\tau_{\mathrm{3D}}/\tau_{\mathrm{p}}}{(1+\tau_{\mathrm{b}}/\tau_{\mathrm{a}})\sinh L/\ell_{\mathrm{sf}}} = \frac{2K''}{\tau_{\mathrm{p}}}\cdot\langle S_z, S_z\rangle$	$\frac{2\tilde{\alpha}\sin\delta\cdot(\tau_{\mathrm{3D}}/\tau_{\mathrm{p}})}{(1+\tau_{\mathrm{b}}/\tau_{\mathrm{a}})\sinh L/\ell_{\mathrm{sf}}} = \frac{2\lambda_{\mathrm{recip}}}{v_{\mathrm{F}}\tau_{\mathrm{p}}} = \frac{2K''}{\tau_{\mathrm{p}}}\cdot\frac{\langle v_z, S_z\rangle}{v_{\mathrm{F}}}$	$\frac{-2\tau_{\mathrm{3D}}/\tau_{\mathrm{p}}}{\sinh L/\ell_{\mathrm{sf}}}\cdot\frac{\tau_{\mathrm{t}}+\tau_{\mathrm{a}}}{\tau_{\mathrm{a}}+\tau_{\mathrm{b}}}$	$\frac{-2\tau_{\mathrm{3D}}}{\tau_{\mathrm{p}}}\cdot\frac{\tau_{\mathrm{c}}}{\tau_{\mathrm{a}}+\tau_{\mathrm{b}}}$	$\frac{\tau_{\mathrm{3D}}}{(\tau_{\mathrm{a}}+\tau_{\mathrm{b}})\sinh L/\ell_{\mathrm{sf}}}$

We then consider other coefficients and linear responses in the EE and IEE. We analytically obtained ratios between typical quantities—electric field applied in the z direction E, 2D spin density s_z, 2D charge current density flowing in the z direction j_c, 3D spin accumulation $\mu_{\mathrm{s}}^{(\mathrm{n})}(y)$ at $y = 0, L$ planes, and 3D spin current density $J_{\mathrm{s}}^{(\mathrm{n})}(y)$ at $y = 0, L$ planes. These ratios are listed in Table II for the EE case and Table III for the IEE case, where we used the following auxiliary variables:

$$\frac{1}{\tau_{\mathrm{a}}} \equiv \left(\frac{1}{\tau_{\mathrm{p}}}+\frac{1}{\tau_{\mathrm{t}}}\right)\tan\delta, \quad \tau_{\mathrm{b}} \equiv \tau_{\mathrm{t}}+\tau_{\mathrm{3D}}\coth\frac{L}{\ell_{\mathrm{sf}}}, \tag{40a}$$

$$\tau_{\mathrm{c}} \equiv \tau_{\mathrm{3D}}+(\tau_{\mathrm{t}}+\tau_{\mathrm{a}})\coth\frac{L}{\ell_{\mathrm{sf}}}, \qquad \tilde{\alpha} \equiv \frac{\alpha}{v_{\mathrm{F}}\hbar}, \tag{40b}$$

$$r \equiv 1+\tilde{\alpha}^2\left(1-\frac{\sin 2\delta}{1+\tau_{\mathrm{b}}/\tau_{\mathrm{a}}}\right). \tag{40c}$$

For example, a current-induced spin polarization coefficient β found in a relation $s_z = \beta j_c$ is obtained in Tables II and III as $\beta_{\mathrm{EE}} = (ev_{\mathrm{F}})^{-1}\cdot 2\tilde{\alpha}\cos\delta/[(1+\tau_{\mathrm{a}}/\tau_{\mathrm{b}})r]$ for the EE, and $\beta_{\mathrm{IEE}} = (ev_{\mathrm{F}}\cdot\tilde{\alpha}\sin\delta)^{-1}$ for the IEE. They are different from each other, reflecting the different nonequilibrium states between the EE and IEE.

C. Reciprocal relationship

We here derive the reciprocal relationship between the EE and IEE within the presented schemes. Let $\mathscr{V}$ be the linear space of $\varphi(\boldsymbol{k},\gamma)$ and $G(\boldsymbol{k},\gamma,\boldsymbol{k}',\gamma')$ be the inverse matrix of $M_{\mathrm{tot}}(\boldsymbol{k},\gamma,\boldsymbol{k}',\gamma')$ in the quotient space $\mathscr{V}/\mathrm{Ker}(M_{\mathrm{tot}})$. Then $\varphi(\boldsymbol{k},\gamma)$ is expressed as

$$\varphi(\boldsymbol{k},\gamma) = \sum_{\boldsymbol{k}',\gamma'} G(\boldsymbol{k},\gamma,\boldsymbol{k}',\gamma')[b_{\mathrm{EE}}(\boldsymbol{k}',\gamma')+b_{\mathrm{IEE}}(\boldsymbol{k}',\gamma')]. \tag{41}$$

The charge current density and spin density are accordingly expressed as

$$\begin{bmatrix} j_z^{\mathrm{c}}/(-e) \\ s_z \end{bmatrix} = \begin{bmatrix} \langle v_z, v_z\rangle & \langle v_z, S_z\rangle \\ \langle S_z, v_z\rangle & \langle S_z, S_z\rangle \end{bmatrix}\begin{bmatrix} (-e)E_z\tau_{\mathrm{p}} \\ K''\cdot J_{\mathrm{s}}^{\mathrm{ext}} \end{bmatrix}, \tag{42}$$

with $K'' = -2K\tau_{\mathrm{p}}/N_0$ [the symbol K has been defined in Eq. (36)]. Here we defined a bilinear form

$$\langle X, Y\rangle \equiv \frac{-1}{V}\sum_{\boldsymbol{k},\gamma,\boldsymbol{k}',\gamma'} X(\boldsymbol{k},\gamma)G(\boldsymbol{k},\gamma,\boldsymbol{k}',\gamma')Y(\boldsymbol{k}',\gamma') \cdot \delta(\epsilon(\boldsymbol{k},\gamma)-\mu_0). \tag{43}$$

As we consider the elastic scattering process, the matrices M_{tot} and its inverse G have nonzero elements only between eigenstates with the same energy. We can thus replace $\epsilon(\boldsymbol{k},\gamma)$ in Eq. (43) by $\epsilon(\boldsymbol{k}',\gamma')$. In addition, M_{tot} is a symmetric matrix and so is its inverse G. The symmetry

$$\langle Y, X\rangle = \langle X, Y\rangle \tag{44}$$

holds accordingly, which leads to equality between cross-coefficients: $\langle S_z, v_z\rangle = \langle v_z, S_z\rangle$. This equality is also expressed as a ratio of quantities on both sides of Eq. (42). We can eliminate a factor K'' from this expression by using a relation for the spin accumulation at the open end $\mu_{\mathrm{s}}^{(\mathrm{n})}(L) = 4Ks_z/N_0$ that holds for the EE. A reciprocal relationship between the EE and IEE is then obtained as

$$\frac{-1}{2}\cdot\frac{\mu_{\mathrm{s}}^{(\mathrm{n})}(L)}{(-e)E}\bigg|_{\mathrm{EE}} = \frac{j_{\mathrm{c}}/(-e)}{J_{\mathrm{s}}^{\mathrm{ext}}}\bigg|_{\mathrm{IEE}} (\equiv \lambda_{\mathrm{recip}}). \tag{45}$$

Here the coefficients on both sides represent nonlocal responses separated by the interface; E and $J_{\mathrm{s}}^{\mathrm{ext}}$ are input, and 2D electric current j_{c} can be detected as a voltage at the

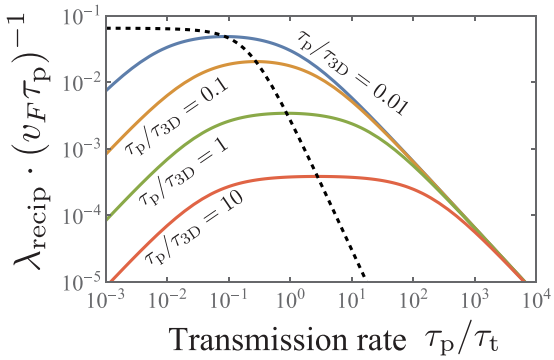

FIG. 5. Linear response specified by the reciprocal relationship of the Edelstein effect $\lambda_{\rm recip}$ for varying the parameters of the interface and 3D metal. The colored lines show different spin diffusion rates in the three-dimensional nonmagnetic metal. The dashed black line shows the peak location of the response with respect to the transmission rate τ_p/τ_t. The parameters are chosen as $(\alpha/v_F\hbar,\, \delta,\, L/\ell_{sf}) = (0.1,\, \pi/64,\, 1)$.

boundary of the 2D metal; the spin accumulation at the edge $\mu_s^{(n)}(L)$ can also be detected by the Kerr effect.

The reciprocal relationship obtained above is a generalization of the reciprocal relationship at the surface derived by Shen *et al.* [5] to the interface system. In their study, the spin current injection in the IEE was treated effectively as a time-dependent magnetic field applying on the surface, though there remained ambiguity to read such external field to the spin current. Our direct calculation on the spin current injection from the 3D metal and resulting reciprocal relationship (45) overcome that difficulty.

The cross-coefficient given by the reciprocal relationship $\lambda_{\rm recip}$ is shown in Fig. 5. It is read that the linear response exhibits nonmonotonic behavior with respect to the transmission rate across the interface τ_p/τ_t, while the smaller spin diffusion rate in the 3D metal τ_p/τ_{3D} gives a larger response. In a low transmission rate $\tau_p/\tau_t \ll 1$, the response across the interface is governed by the spin transmission rate into or out of the 3D metal with finite thickness $(\tau_t + \tau_{3D}\coth L/\ell_{sf})^{-1}$, as the same as q_{EE}. Then we find $\lambda_{\rm recip} \sim q_{EE}\cdot[\mu_s^{(n)}(L)/J_s^{(n)}(0)]_{EE} \sim \tau_{3D}/(\tau_t \sinh L/\ell_{sf} + \tau_{3D}\cosh L/\ell_{sf})$, which explains the behavior of $\lambda_{\rm recip}$ in $\tau_p/\tau_t \ll 1$. In a high transmission rate $\tau_p/\tau_t \gg 1$, on the other hand, the bottleneck of the response is the Edelstein effect or its inverse at the 2D metal, which is roughly represented as the modified relaxation time in the 2D metal by the interface transmission $(1/\tau_p + 1/\tau_t)^{-1}$. We thus find $\lambda_{\rm recip} \sim (1/\tau_p + 1/\tau_t)^{-1}$ in $\tau_p/\tau_t \gg 1$. The response $\lambda_{\rm recip}$ is maximal in the intermediate region, accordingly.

As the cross-coefficient given by the reciprocal relationship can be measured directly, $\lambda_{\rm recip}$ is an experimentally important ratio as well as q_{EE} and λ_{IEE}.

We close this section by showing another representation of the reciprocal relationship that captures the essence of the composite system we have considered. That is obtained by arranging the original linear transformation between the external forces $(E,\, J_s^{(n)}(L))$ and responses $(j_c,\, \mu^{(n)}(L))$ into a new linear transformation between the pairs at both sides of the system $(\mu_s^{(n)}(L),\, J_s^{(n)}(L))$ and $(E,\, j_c)$:

$$\begin{bmatrix}\mu_s^{(n)}(L)/2\\ -J_s^{(n)}(L)\end{bmatrix} = \begin{bmatrix}\cosh L/\ell_{sf} & \frac{e^2\ell_{sf}}{\sigma^{(n)}}\sinh L/\ell_{sf}\\ \frac{\sigma^{(n)}}{e^2\ell_{sf}}\sinh L/\ell_{sf} & \cosh L/\ell_{sf}\end{bmatrix}\begin{bmatrix}\mu_s^{(n)}(0)/2\\ -J_s^{(n)}(0)\end{bmatrix}, \qquad \begin{bmatrix}\mu_s^{(n)}(0)/2\\ -J_s^{(n)}(0)\end{bmatrix} = \begin{bmatrix}Q_{11} & Q_{12}\\ Q_{21} & Q_{22}\end{bmatrix}\begin{bmatrix}(-e)E\\ j_c/(-e)\end{bmatrix}. \tag{46}$$

Here the former represents the spin diffusion equation in the 3D metal, while the latter indicates a local charge-spin conversion at the interface. The matrix elements Q_{ij} are calculated based on the coefficients in Tables II and III as

$$Q_{11} = (1 + Q_{12}Q_{21})/Q_{22}, \tag{47a}$$
$$Q_{12} = -(1 + \tau_t/\tau_a)/(v_F N_0\tilde{\alpha}\sin\delta), \tag{47b}$$
$$Q_{21} = (1 + \tilde{\alpha}^2)v_F N_0/(2\tilde{\alpha}\cos\delta), \tag{47c}$$
$$Q_{22} = -(v_F\tau_a\tilde{\alpha}\sin\delta)^{-1} = -\lambda_{IEE}^{-1}. \tag{47d}$$

The Onsager reciprocity (45) is equivalent to that the determinant of each matrix above is equal to 1, in particular $\det Q = 1$.

Moreover, the transfer matrix method expressed in Eqs. (46) serves as a powerful tool for computing transport coefficients via the Edelstein effect in the composite systems. First, by using Eqs. (46) and the matrix elements Q_{ij}, we can derive not only the spin current–to–charge current conversion efficiency $\lambda_{IEE} = -Q_{22}^{-1}$ but also the charge current–to–spin current conversion efficiency and cross-coefficient

$$q_{EE} = \left|Q_{11} + Q_{21}\cdot\frac{e^2\ell_{sf}}{\sigma^{(n)}}\coth\frac{L}{\ell_{sf}}\right|^{-1}, \tag{48a}$$
$$\lambda_{\rm recip} = -\left[Q_{12}\cdot\frac{\sigma^{(n)}}{e^2\ell_{sf}}\sinh\frac{L}{\ell_{sf}} + Q_{22}\cosh\frac{L}{\ell_{sf}}\right]^{-1}. \tag{48b}$$

The matrix elements Q_{ij} thus play a fundamental role in the conversion ratio of the Edelstein effect. Second, Eqs. (46) allow us to consistently describe the EE and IEE not depending on the choice of controllable parameters. For example, we can regard $(E,\, \mu_s^{(n)}(0))$, not $(E,\, J_s^{(n)}(L))$, as a set of independent variables in Eqs. (46), i.e., input for the EE and IEE, which is consistent with the previous studies [8,9]. Third, the transfer matrix method is useful for systematic calculations of transport coefficients when another system, such as a spin Hall material, is attached on the $y = L$ plane [shown in Figs. 1(b) and 1(c)]. In that new composite system, another transfer matrix would be multiplied to the vector at $y = L$ plane $(\mu_s^{(n)}(L)/2,\, -J_s^{(n)}(L))$, which relates other parameters at another end of the attached system.

IV. DISCUSSION

We have presented a theoretical scheme capable of dealing with spin relaxation, nonlocal spin transport of a metal with strong SOC and charge-spin interconversion at an interface between a metal with strong SOC and a nonmagnetic metal. Our model and results have an advantage in that the calculations on the spin relaxation times, spin diffusion lengths, and coefficients found in the Edelstein effect at the chiral metal interface can be interpreted as the counterparts of the spin

transport in the 2D systems with the Rashba SOC or Rashba-Dresselhaus SOC. In particular, the analytical solution for the composite system beyond the relaxation time approximation will help us to understand and control spin transport through the interface between those 2D systems and metals.

We now focus on the application of our theory to experiments. In particular, we consider how we can make use of the obtained reciprocal relationship for the Edelstein effect in the composite systems. We then discuss how to formulate the theory more consistently with the experiments on spin transport in chiral metals [15,17,18].

There are various applications for experiments stemmed from the Onsager reciprocity that we have both formulated and analytically calculated. First, we can make use of that reciprocal relationship (45) as a measure of accuracy of experiments on the direct and inverse Edelstein effect across the interface. Furthermore, we can estimate the SOC parameters at the chiral metal surface ($\alpha_\parallel$ and $\alpha_\perp$) from the cross-coefficient $\lambda_{\rm recip}$ by the following procedure.

When the 3D metal attached on the chiral metal is thin enough to satisfy both $L/\ell_{\rm sf} \ll 1$ and $L/\ell_{\rm sf} \ll \tau_{\rm 3D}/\tau_{\rm t}$, we find that $\lambda_{\rm recip} \simeq \lambda_{\rm IEE}/(\cosh L/\ell_{\rm sf}) \simeq \lambda_{\rm IEE}[1-(L/\ell_{\rm sf})^2/2]$ holds according to Eq. (48b) and Table III. A ratio between $\lambda_{\rm recip}$ and electrical conductivity in the case of the direct Edelstein effect (shown in Table II) is then written as

$$\frac{\lambda_{\rm recip}}{(j_{\rm c}/E)|_{\rm EE}} \simeq \frac{\lambda_{\rm IEE}}{(j_{\rm c}/E)|_{\rm EE}/r}\left[1-\frac{1}{2}\left(\frac{L}{\ell_{\rm sf}}\right)^2\right] \tag{49}$$

$$= \frac{2\pi\hbar}{e^2}\frac{\alpha_\parallel}{\epsilon_{\rm F}}\left[1-\frac{1}{2}\left(\frac{L}{\ell_{\rm sf}}\right)^2\right] \tag{50}$$

with $r = 1 + O(\alpha/v_{\rm F}\hbar)^2 \simeq 1$. We can read the SOC parameter $\alpha_\parallel$ from the relation above if we know $L/\ell_{\rm sf}$ of the 3D metal, the electrical conductivity $(j_{\rm c}/E)|_{\rm EE}$ and Fermi level $\epsilon_{\rm F}$ in the chiral metal surface, and the cross-coefficient due to the Edelstein effect $\lambda_{\rm recip}$. Here we can directly measure both $(j_{\rm c}/E)|_{\rm EE}$ and $\lambda_{\rm recip}$ since they are ratios of input to output in the composite system. We can also estimate the other SOC parameter $\alpha_\perp$ if we replace spin polarization and electrical conductivity in the z direction with those in the x direction.

Our analytical calculations also provide a way to enhance the cross-coefficient $\lambda_{\rm recip}$. Figure 5 and Eq. (48b) show that $\lambda_{\rm recip}$ increases as the ratio $\tau_{\rm p}/\tau_{\rm 3D} = \sigma^{(\rm n)}\tau_{\rm p}/(e^2\ell_{\rm sf}N_0)$ decreases to zero. In other words, for a given chiral metal or other 2D spin-splitting systems, we can efficiently measure the response of both direct and inverse Edelstein effect, represented by $\lambda_{\rm recip}$, by adopting a 3D nonmagnetic metal with long spin diffusion length $\ell_{\rm sf}$ or low electrical conductivity $\sigma^{(\rm n)}$.

We now discuss future prospects in more accurately describing the experimental situation of spin transport in chiral metals. An important direction of a future study is an application/generalization of the present scheme to the 3D chiral metal with the SOC expressed as $\alpha_\parallel k_z\sigma_z + \alpha_\perp(k_x\sigma_x + k_y\sigma_y)$. It will unravel the underlying mechanisms in transport properties found in [15,17,18].

In generalizing the scheme in Sec. III to the bulk chiral metals, along with the experimental setup, we need to calculate the spatial distribution of the charge current density and spin density in the chiral metal from the interior to the interface with another nonmagnetic metal, which may describe charge-spin interconversion more consistently with the experiments.

Along the experimental situations, we have to consider also spin-flip scattering process, which we neglected at the surface in the present study. It can contribute to these spin relaxation time and spin diffusion length of the conduction electrons in general. That scattering process is due to spin-orbit interaction from impurity potentials, lattice vibrations, and the hyperfine interaction [51,53,54].

V. CONCLUSIONS

We have described spin transport in a spin-splitting model of the chiral metal surface and interface, making full use of the Boltzmann transport equation beyond the relaxation time approximation. The condition if we can safely use the Boltzmann transport equation for that two-band system is also discussed based on the Keldysh formalism in the Supplemental Material [27], which endorses the validity of the following results. We have first extracted slow modes responsible for spin relaxation and spin diffusion in the surface, respecting conservation laws. That enables us to define spin relaxation time and spin diffusion length without using the conventional idea of spin-dependent chemical potentials. Our definition applies to the systems with strong spin-orbit coupling in the clean limit when the Edelstein effect becomes evident, and it will serve as a foundation for discussing the nonlocal spin transport in the bulk chiral metal. We have then clearly addressed the charge-spin interconversion efficiency at the interface, which has been treated phenomenologically in previous studies. In particular, we have derived the analytical expression for the charge current–to–spin current conversion efficiency $q_{\rm EE}$, which is found to depend on the details of the 3D nonmagnetic metal attached on the chiral metal surface. We have finally developed the Onsager reciprocal relationship for the Edelstein effect (45) that relates local input and local output spatially separated by the interface. Comparing the Edelstein effect and its inverse effect, their distribution functions help us to understand the nonequilibrium states. In addition, expressions for various transport coefficients that we have obtained analytically would provide a powerful tool to evaluate the accuracy of measurements of the Edelstein effect, or to calculate what cannot be measured directly in the Edelstein effect.

ACKNOWLEDGMENTS

We are grateful to Y. Togawa, H. Shishido, J. Ohe, Y. Fuseya, and T. Kato for constructive discussions on the subject. We wish to thank J. Kishine, H. M. Yamamoto, H. Kusunose, E. Saitoh, and S. Sumita for their helpful comments. Y.S. is supported by World-leading Innovative Graduate Study Program for Materials Research, Industry, and Technology (MERIT-WINGS) of the University of Tokyo. Y.S. is also supported by JSPS KAKENHI Grant No. JP22J12348. Y.K. is supported by JSPS KAKENHI Grants No. JP20K03855 and No. JP21H01032. This research was supported by a Special Project by the Institute for Molecular Science (IMS Program No. 21-402).

[1] V. M. Edelstein, Spin polarization of conduction electrons induced by electric current in two-dimensional asymmetric electron systems, Solid State Commun. **73**, 233 (1990).

[2] A. G. Aronov and Yu B. Lyanda-Geller, Nuclear electric resonance and orientation of carrier spins by an electric field, Pis'ma Zh. Eksp. Teor. Fiz. **50**, 398 (1989) [JETP Lett. **50**, 431 (1989)].

[3] Y. K. Kato, R. C. Myers, A. C. Gossard, and D. D. Awschalom, Current-Induced Spin Polarization in Strained Semiconductors, Phys. Rev. Lett. **93**, 176601 (2004).

[4] S. D. Ganichev, E. L. Ivchenko, V. V. Bel'Kov, S. A. Tarasenko, M. Sollinger, D. Weiss, W. Wegscheider, and W. Prettl, Spin-galvanic effect, Nature (London) **417**, 153 (2002).

[5] K. Shen, G. Vignale, and R. Raimondi, Microscopic Theory of the Inverse Edelstein Effect, Phys. Rev. Lett. **112**, 096601 (2014).

[6] R. H. Silsbee, Spin-orbit induced coupling of charge current and spin polarization, J. Phys.: Condens. Matter **16**, R179 (2004).

[7] P. Gambardella and I. M. Miron, Current-induced spin-orbit torques, Philos. Trans. R. Soc. A **369**, 3175 (2011).

[8] S. Zhang and A. Fert, Conversion between spin and charge currents with topological insulators, Phys. Rev. B **94**, 184423 (2016).

[9] R. Dey, N. Prasad, L. F. Register, and S. K. Banerjee, Conversion of spin current into charge current in a topological insulator: Role of the interface, Phys. Rev. B **97**, 174406 (2018).

[10] J. C. Rojas-Sánchez, L. Vila, G. Desfonds, S. Gambarelli, J. P. Attané, J. M. De Teresa, C. Magén, and A. Fert, Spin-to-charge conversion using Rashba coupling at the interface between non-magnetic materials, Nat. Commun. **4**, 2944 (2013).

[11] H. J. Zhang, S. Yamamoto, B. Gu, H. Li, M. Maekawa, Y. Fukaya, and A. Kawasuso, Charge-to-Spin Conversion and Spin Diffusion in Bi/Ag Bilayers Observed by Spin-Polarized Positron Beam, Phys. Rev. Lett. **114**, 166602 (2015).

[12] E. Lesne, Y. Fu, S. Oyarzun, J. C. Rojas-Sánchez, D. C. Vaz, H. Naganuma, G. Sicoli, J.-P. Attané, M. Jamet, E. Jacquet, J.-M. George, A. Barthélémy, H. Jaffrès, A. Fert, M. Bibes, and L. Vila, Highly efficient and tunable spin-to-charge conversion through Rashba coupling at oxide interfaces, Nat. Mater. **15**, 1261 (2016).

[13] Y. Shiomi, K. Nomura, Y. Kajiwara, K. Eto, M. Novak, K. Segawa, Y. Ando, and E. Saitoh, Spin-Electricity Conversion Induced by Spin Injection into Topological Insulators, Phys. Rev. Lett. **113**, 196601 (2014).

[14] J.-C. Rojas-Sánchez, S. Oyarzún, Y. Fu, A. Marty, C. Vergnaud, S. Gambarelli, L. Vila, M. Jamet, Y. Ohtsubo, A. Taleb-Ibrahimi, P. Le Fèvre, F. Bertran, N. Reyren, J.-M. George, and A. Fert, Spin to Charge Conversion at Room Temperature by Spin Pumping into a New Type of Topological Insulator: α-Sn Films, Phys. Rev. Lett. **116**, 096602 (2016).

[15] A. Inui, R. Aoki, Y. Nishiue, K. Shiota, Y. Kousaka, H. Shishido, D. Hirobe, M. Suda, J.-I. Ohe, J.-I. Kishine, H. M. Yamamoto, and Y. Togawa, Chirality-Induced Spin-Polarized State of a Chiral Crystal $CrNb_3S_6$, Phys. Rev. Lett. **124**, 166602 (2020).

[16] Y. Nabei, D. Hirobe, Y. Shimamoto, K. Shiota, A. Inui, Y. Kousaka, Y. Togawa, and H. M. Yamamoto, Current-induced bulk magnetization of a chiral crystal $CrNb_3S_6$, Appl. Phys. Lett. **117**, 052408 (2020).

[17] K. Shiota, A. Inui, Y. Hosaka, R. Amano, Y. Onuki, M. Hedo, T. Nakama, D. Hirobe, J.-I. Ohe, J.-I. Kishine, H. M. Yamamoto, H. Shishido, and Y. Togawa, Chirality-Induced Spin Polarization over Macroscopic Distances in Chiral Disilicide Crystals, Phys. Rev. Lett. **127**, 126602 (2021).

[18] H. Shishido, R. Sakai, Y. Hosaka, and Y. Togawa, Detection of chirality-induced spin polarization over millimeters in polycrystalline bulk samples of chiral disilicides $NbSi_2$ and $TaSi_2$, Appl. Phys. Lett. **119**, 182403 (2021).

[19] Note that the observed spin polarization unique to the chiral metals cannot be explained as a linear spin Hall effect, as described in Ref. [25]. The spin Hall conductivity relates spin current and electric field, which are odd under spatial inversion. It follows that the spin Hall conductivity itself is independent of whether the spatial inversion is included in the point group or not; in particular, no linear spin Hall effect is unique to chiral crystals. More precisely, in the point group 622 without magnetic orders, spin Hall conductivity vanishes when the electric field and spin polarization direction are parallel [55]. The spin Hall effect is thus unrelated to the observed spin polarization that is parallel to the applied electric field.

[20] T. Furukawa, Y. Watanabe, N. Ogasawara, K. Kobayashi, and T. Itou, Current-induced magnetization caused by crystal chirality in nonmagnetic elemental tellurium, Phys. Rev. Res. **3**, 023111 (2021).

[21] T. Yoda, T. Yokoyama, and S. Murakami, Current-induced orbital and spin magnetizations in crystals with helical structure, Sci. Rep. **5**, 12024 (2015).

[22] P. A. Frigeri, Superconductivity in crystals without an inversion center, Ph.D. thesis, ETH-Zürich, 2005.

[23] T. Furukawa, Y. Shimokawa, K. Kobayashi, and T. Itou, Observation of current-induced bulk magnetization in elemental tellurium, Nat. Commun. **8**, 954 (2017).

[24] G. Tatara, Nonlocality of electrically-induced spin accumulation in chiral metals, J. Phys. Soc. Jpn. **91**, 073701 (2022).

[25] A. Roy, F. T. Cerasoli, A. Jayaraj, K. Tenzin, M. B. Nardelli, and J. Sławińska, Long-range current-induced spin accumulation in chiral crystals, npj Comput. Mater. **8**, 243 (2022).

[26] T. Valet and A. Fert, Theory of the perpendicular magnetoresistance in magnetic multilayers, Phys. Rev. B **48**, 7099 (1993).

[27] See Supplemental Material at http://link.aps.org/supplemental/10.1103/PhysRevB.107.115305 for supporting information: relations between our model and other SOC models, details of the Boltzmann equation analysis in Sec. II, microscopic derivation of the Boltzmann equation and transmission rate across the interface with arbitrary spin polarization in terms of the Keldysh Green's function, review of the Valet-Fert solution, derivation of the effective Boltzmann equation at the interface in Sec. III, analytical expressions of electron distributions for Edelstein effect and its inverse, and dependence on the thickness of the three-dimensional metal, omitted in this main text.

[28] J. Rammer and H. Smith, Quantum field-theoretical methods in transport theory of metals, Rev. Mod. Phys. **58**, 323 (1986).

[29] M. Levanda and V. Fleurov, A Wigner quasi-distribution function for charged particles in classical electromagnetic fields, Ann. Phys. **292**, 199 (2001).

[30] T. Kita, Gauge invariance and Hall terms in the quasiclassical equations of superconductivity, Phys. Rev. B **64**, 054503 (2001).

[31] S. Onoda, N. Sugimoto, and N. Nagaosa, Theory of non-equilibirum states driven by constant electromagnetic fields, Prog. Theor. Phys. **116**, 61 (2006).

[32] M. I. D'yakonov and A. V. Khaetskii, Relaxation of nonequilibrium carrier-density matrix in semiconductors with degenerate bands, Zh. Eksp. Teor. Fiz **86**, 1843 (1984) [Sov. Phys. JETP **59**, 1072 (1984)].

[33] A. Khaetskii, Nonexistence of Intrinsic Spin Currents, Phys. Rev. Lett. **96**, 056602 (2006).

[34] A. V. Shytov, E. G. Mishchenko, H.-A. Engel, and B. I. Halperin, Small-angle impurity scattering and the spin Hall conductivity in two-dimensional semiconductor systems, Phys. Rev. B **73**, 075316 (2006).

[35] J. Kailasvuori, Boltzmann approach to the spin Hall effect revisited and electric field modified collision integrals, J. Stat. Mech. (2009) P08004.

[36] T. Jungwirth, Q. Niu, and A. H. MacDonald, Anomalous Hall Effect in Ferromagnetic Semiconductors, Phys. Rev. Lett. **88**, 207208 (2002).

[37] M. Onoda and N. Nagaosa, Topological nature of anomalous Hall effect in ferromagnets, J. Phys. Soc. Jpn. **71**, 19 (2002).

[38] W. Kohn and J. M. Luttinger, Quantum theory of electrical transport phenomena, Phys. Rev. **108**, 590 (1957).

[39] J.-I. Inoue, G. E. W. Bauer, and L. W. Molenkamp, Suppression of the persistent spin Hall current by defect scattering, Phys. Rev. B **70**, 041303(R) (2004).

[40] H. Isshiki, P. Muduli, J. Kim, K. Kondou, and Y. C. Otani, Phenomenological model for the direct and inverse Edelstein effects, Phys. Rev. B **102**, 184411 (2020).

[41] G. Dresselhaus, Spin-orbit coupling effects in zinc blende structures, Phys. Rev. **100**, 580 (1955).

[42] R. Winkler, *Spin-Orbit Coupling Effects in Two-Dimensional Electron and Hole Systems*, Springer Tracts in Modern Physics (Springer, Berlin, 2003), Vol. 191.

[43] Y. Ōnuki, A. Nakamura, T. Uejo, A. Teruya, M. Hedo, T. Nakama, F. Honda, and H. Harima, Chiral-structure-driven split Fermi surface properties in $TaSi_2$, $NbSi_2$, and VSi_2, J. Phys. Soc. Jpn. **83**, 061018 (2014).

[44] R. Oiwa and H. Kusunose, Rotation, Electric-Field Responses, and Absolute Enantioselection in Chiral Crystals, Phys. Rev. Lett. **129**, 116401 (2022).

[45] Yu A. Bychkov and É. I. Rashba, Properties of a 2D electron gas with lifted spectral degeneracy, Pis'ma Zh. Eksp. Teor. Fiz. **39**, 66 (1984) [JETP Lett. **39**, 78 (1984)].

[46] Our SOC model can also be converted to a 2D system with both Rashba and Dresselhaus SOCs under appropriate rotations (Sec. S1 of the Supplemental Material [27]).

[47] R. H. Silsbee, Theory of the detection of current-induced spin polarization in a two-dimensional electron gas, Phys. Rev. B **63**, 155305 (2001).

[48] Such an extremely slowly decaying mode stems from the conservation of charge.

[49] L. Szolnoki, B. Dóra, A. Kiss, J. Fabian, and F. Simon, Intuitive approach to the unified theory of spin relaxation, Phys. Rev. B **96**, 245123 (2017).

[50] R. J. Elliott, Theory of the effect of spin-orbit coupling on magnetic resonance in some semiconductors, Phys. Rev. **96**, 266 (1954).

[51] Y. Yafet, *g* factors and spin-lattice relaxation of conduction electrons, in *Solid State Physics*, Advances in Research and Applications, edited by F. Seitz and D. Turnbull (Academic Press, New York, 1963), Vol. 14, pp. 1–98.

[52] M. I. D'yakonov and V. I. Perel', Spin relaxation of conduction electrons in noncentrosymmetric semiconductors, Fiz. Tverd. Tela **13**, 3581 (1971) [Sov. Phys. Solid State **13**, 3023 (1972)].

[53] A. W. Overhauser, Paramagnetic relaxation in metals, Phys. Rev. **89**, 689 (1953).

[54] I. Žutić, J. Fabian, and S. Das Sarma, Spintronics: Fundamentals and applications, Rev. Mod. Phys. **76**, 323 (2004).

[55] M. Seemann, D. Ködderitzsch, S. Wimmer, and H. Ebert, Symmetry-imposed shape of linear response tensors, Phys. Rev. B **92**, 155138 (2015).